Segmentation and Holocene Behavior of the Middle Strand of the North Anatolian Fault (NW Turkey)

Y. Benjelloun[1], J. de Sigoyer[2], S. Garambois[2], J. Carcaillet[2], and Y. Klinger[1]

[1]Université de Paris, Institut de physique du globe de Paris, CNRS, F-75005 Paris, France.

[2]Univ. Grenoble Alpes, Univ. Savoie Mont Blanc, CNRS, IRD, IFSTTAR, ISTerre, 38000 Grenoble, France.

Corresponding author: Yacine Benjelloun (benjelloun@ipgp.fr)

Key Points:

- Systematic measurements of horizontal cumulative offsets along the middle strand of the North Anatolian fault

- Statistical analysis of the dataset allows to identify the last large ruptures along the fault and the associated slip per-segment

- Comparison with independent constraints on past earthquakes leads to discuss past rupture scenarios

Abstract

The North Anatolian fault in the Marmara region is composed of three parallel strands all separated by ~50 km. The activity of the middle strand, which borders the southern edge of the Marmara Sea, is much debated because of its present-day very low seismicity. This contrasts with historical, archaeological and paleoseismological evidence, which suggest several destructive earthquakes have occurred during the last 2000 years. Our study aims to better constrain seismic hazard on the middle strand by exploring its Holocene paleoseismicity. For this, we mapped 148 km of the eastern part of the middle strand, using high-resolution satellite imagery. A series of landforms offset by the middle strand activity have been systematically measured to recover the past ruptures. Three Late Pleistocene-Holocene terraces have been dated with the terrestrial cosmogenic nuclide method, constraining a horizontal slip rate of $4.4^{+10.6}_{-2.8}$ mm/yr. The statistical analysis of the offsets evidences several major ruptures preserved in the landscape, with coseismic lateral displacements ranging between 3 and 6.5 m. This corresponds to Mw ~7.3 earthquakes able to propagate along several fault segments. Historical seismicity and paleoseismology data suggest that the last large earthquakes along the MNAF happened in 1065 CE and between the 14th and 18th centuries CE. Since then, the MNAF may have accumulated enough stress to generate a destructive rupture.

1 Introduction

Seismic hazard in the highly inhabited areas of northwestern Turkey is mainly related to the activity of the North Anatolian fault (NAF), a ~1500-km long, dextral strike-slip structure that accommodates the relative motion between the Eurasian and Anatolian blocks (Ambraseys, 1970; Barka, 1992; Ketin, 1969; Sengör & Zabci, 2019; Sengör et al., 2005), with a total

geodetic slip estimated around 3 cm/yr (Fig. 1; McClusky et al., 2000; Meade et al., 2002). During the 20th century, the NAF ruptured almost entirely during a westward sequence of major earthquakes from Erzincan, in 1939, to Düzce and Izmit, in 1999 (Akyüz et al., 2002; Ambraseys, 2001a; Barka, 1996; Barka et al., 2002; Hubert-Ferrari et al., 2000; Stein et al., 1997). A seismic gap remains in the Sea of Marmara, in front of Istanbul, where a major earthquake is expected to occur in the next decades (Parsons et al., 2000). In addition to the main northern strand of the NAF, one should also consider the seismic hazard due to the presence of two secondary strands known as the middle and southern strands (MNAF and SNAF, Fig. 1). Although there are a large number of geodetic and geological slip rate estimates for the NNAF in the Marmara region (e.g. Dikbas et al., 2018; Ergintav et al., 2014; Grall et al., 2013; Kurt et al., 2013; Motagh et al., 2007; Reilinger et al., 2006), there are few studies for the southern strands (Zabci, 2019). These strands could together accommodate as much as 25% of the total slip of the NAF (Armijo et al., 2002; Flerit et al., 2003), with slip rates between 7 and less than 1 mm/yr on the MNAF estimated with geodetical (Ergintav et al., 2014; Özbey et al., 2021; Reilinger et al., 2006) and geological data (Gasperini et al., 2011; Özalp et al., 2013; Vardar et al., 2014). While the SNAF experienced a Mw 7.2 earthquake in 1953 (Ketin & Rösli, 1953; Kürçer et al., 2008, 2019), no major earthquake ruptured the MNAF during the instrumental period, and the seismicity of the MNAF zone during the last eight decades does not include more than a couple of earthquakes larger than Mw 5. The microseismicity recently recorded has been mostly located west of Iznik Lake and around the Gulf of Gemlik, while the other segments in the east have been characterized by much fewer events and appear quiescent compared with the neighboring NAF strands (Baris et al., 2002; Gürbüz et al., 2000; Öztürk et al., 2009; Tsukuda et al., 1988). These observations explain that the middle strand has often been overlooked in the assessment of deformation of the Marmara region (Le Pichon et al., 2014). This current quiescence contrasts

with a significant historical seismic activity documented by several chronicles mentioning the destruction of Iznik and other surrounding cities located close to the MNAF during large earthquakes occurring in the last 2000 years (Ambraseys, 2002, 2009; Ambraseys & Finkel, 1991; Ambraseys & Jackson, 1998; Guidoboni & Comastri, 2005; Fig. 2).
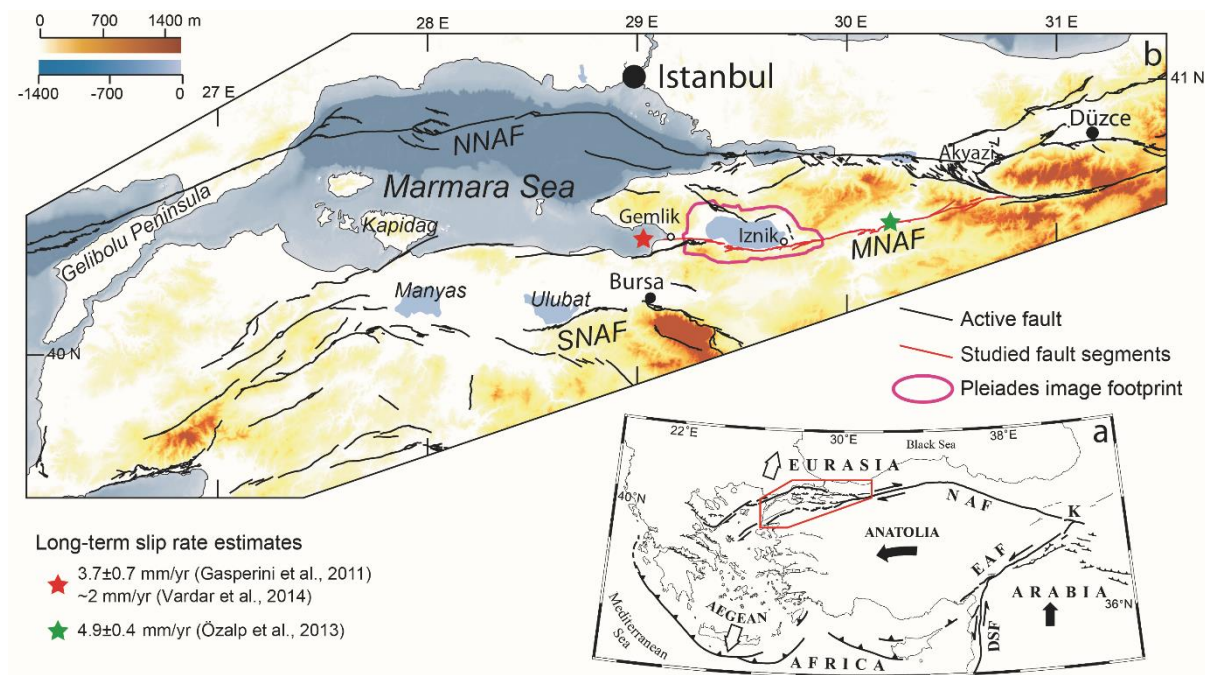

Figure 1. General tectonic context. (a) Schematic map of the main active fault zones of the Eastern Mediterranean (Armijo et al., 1999). NAF = North Anatolian fault, EAF = East Anatolian fault, DSF = Dead Sea fault. The red box surrounds the Marmara region. (b) Main active faults located within the Marmara region in black. The fault map was modified from Emre et al. (2011). NNAF, MNAF and SNAF refers to the northern, middle and southern strand of the NAF respectively. The bathymetry comes from the EMODnet Bathymetry Consortium (2018). The color stars locate fault sections where slip rates were estimated by geology or geomorphology studies (see Section 3 for details).
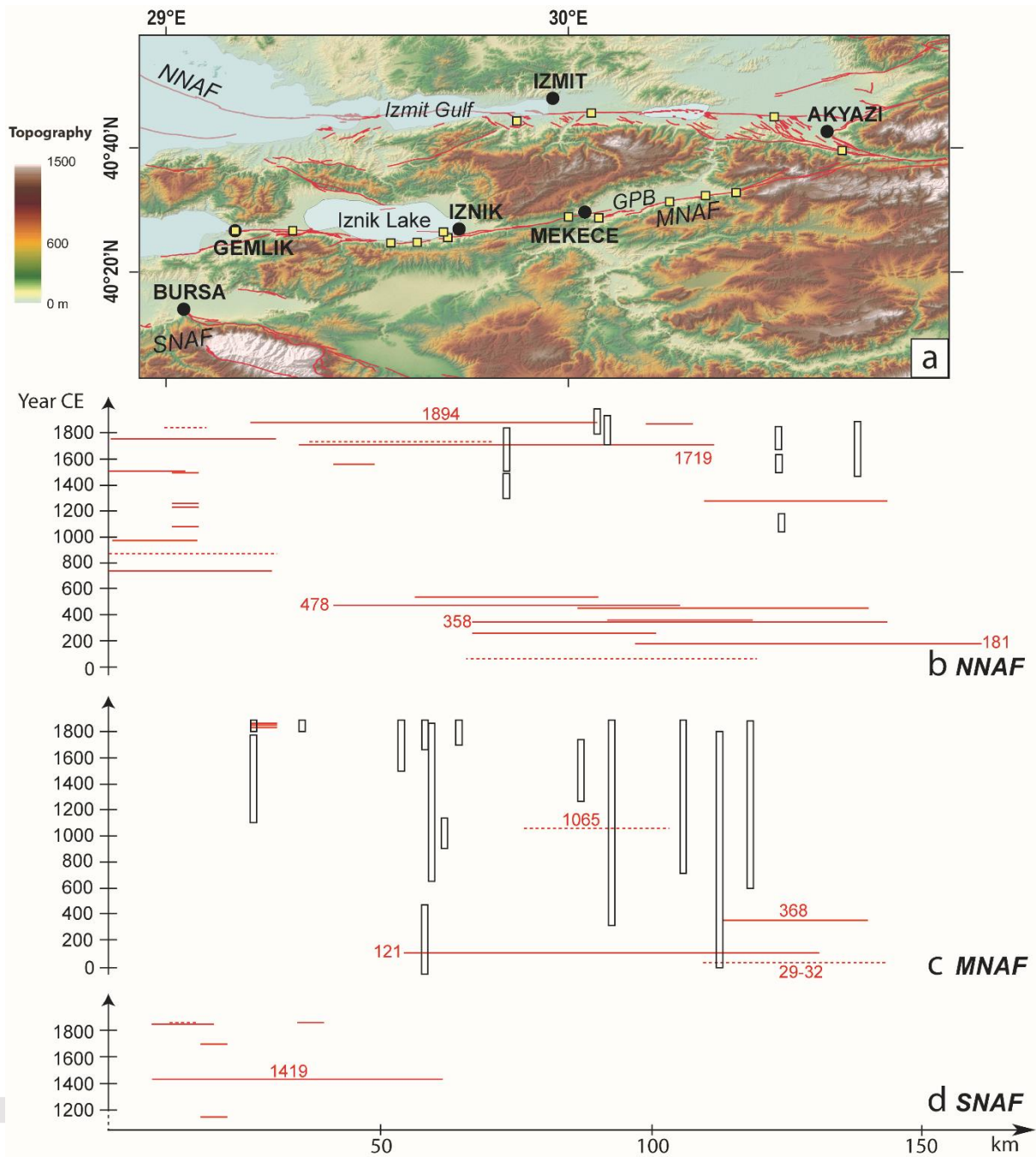
Figure 2. Historical seismicity of the eastern Marmara region before 1900 CE (Common Era).

(a) Active faults and main geographic features of the Marmara region. Trench sites are located

with yellow boxes. GPB=Geyve-Pamukova Basin. (b, c, d) Historical earthquakes (horizontal

red lines) and seismic events documented in palaeoseismological studies (vertical boxes)

along the three strands of the NAF. The horizontal lines are positioned according to the

epicentral areas interpreted from the sources. These epicentral areas are determined from the

spatial distribution of the seismic intensities interpreted from historical descriptions, and their accuracy depends on the availability and quality of the written archives (Ambraseys et al., 2002). Dashed lines indicate less documented events. The length of each horizontal line corresponds to the approximate rupture length of the earthquake. To estimate this length, we rely on the magnitude estimated by historical seismology studies (see Table S1 in Supporting Information), from which a surface rupture length was derived using the relationship of Wells and Coppersmith (1984). The length of the vertical boxes corresponds to the dating of the events within 2σ uncertainty (Civico et al., 2021; Dikbas et al., 2018; Dogan, 2010; Gastineau et al., 2021; Honkura & Isikara, 1991; Ikeda, Suzuki et al., 1991; Klinger et al., 2003; Özalp et al., 2013; Rockwell et al., 2009; see Table S2 in Supporting Information for detailed data).

In the last decades, the development of high-resolution satellite imagery has made it possible to measure the deformation and characterize in great detail the geomorphology of tectonically active regions on a large scale (Elliott et al., 2016; Fu et al., 2004; Klinger et al., 2011; Ren et al., 2018). These images enable us to accurately map active faults along several tens of kilometers, to describe their segmentation and therefore provide useful information on the possible extension of a given rupture (e.g. Ansberque et al., 2016; Choi et al., 2018; Klinger et al., 2005). Such data also make it possible to document the long-term, cumulative slip distribution along the fault through inventories of offset geomorphological markers. This approach has been successfully employed since the 1960s on various faults to extract coseismic slip values from cumulative offset measurements, and to discuss the impact of segmentation in modulating the cumulative along-strike displacement (Ansberque et al., 2016; Barka, 1996; Manighetti et al., 2015, 2020; McGill and Rubin, 1999; Sieh and Jahns, 1984; Zielke et al., 2015; Kurtz et al., 2018).

In this study, we use a set of high-resolution images and topography measurements obtained

from Pleiades data to map the eastern part of the MNAF between Gemlik and Akyazi district (Fig. 2a), and to measure a series of lateral displacements recorded by geomorphological markers, mainly stream talwegs and risers. To gather additional age control on the observed cumulative deformation, we sample and date three levels of wave-cut terraces formed around Iznik Lake. This enables us to constrain a Holocene horizontal slip rate for the central section of the MNAF. A statistical analysis of the offset measurements allows us to extract coseismic displacements for several of the largest past earthquakes and to discuss the slip distribution generated along the fault during these earthquakes. Comparison of these data with the historical seismicity record and previous paleoseismological data shows that this approach is not sensitive enough to detect the smaller events (Mw 6.8-7) that are also known to occur along the MNAF. We finally explore the implications of several plausible scenarios to explain past slip history at the scale of the NAF system east of the Marmara Sea.

2 Geological context: the NAF in the Marmara region

The formation of the NAF initiated some 11-13 Ma ago within a wider pre-existing shear zone which progressively localized through time (Sengör et al., 2005, 2014). Starting possibly from eastern Anatolia, the fault zone grew by westward propagation through the lithosphere over ~10 Ma and reached the northern Aegean between 5 and 1 Ma ago (Armijo et al., 1996, 1999; Barka, 1992). From the Messinian and during the Pliocene, the NAF has functioned as a narrow zone, cutting through and deforming several basins inherited from the previous tectonic stages (Barka, 1992; Yılmaz et al., 1995). While the deformation is localized in a narrow zone in the eastern and central part of the NAF, it is structured on a wider area west of Düzce with a distribution of the deformation across several strands (Armijo et al., 1999; Fig. 1). The NAF strands show oblique kinematics, with local complex partitioning of the

deformation between dextral strike-slip and extensional regimes (Koçyigit & Özacar, 2003). The main northern strand (NNAF) continues along the strike of the main fault zone and crosses the northern part of the Marmara Sea from the Gulf of Izmit to Gelibolu Peninsula (Fig. 1). West of Akyazi district, another fault zone branches off from the NNAF, bounds to the south two successive basins known as the Geyve-Pamukova Basin and Iznik Lake, and reaches the south of the Marmara Sea through the Gulf of Gemlik as a single strand, which we term the middle strand of the NAF (MNAF) (Fig. 3a). West of Gemlik, this fault zone diffuses to a wider region (Sengör & Zabci, 2019; Sengör et al., 2005). Between the Gemlik Gulf and the Kapidag peninsula, the active deformation seems to distribute across two parallel fault strands. While the MNAF continues along the southern shore of Marmara, a southern fault strand (SNAF) continues west-southwestwards to Ulubat and Manyas Lakes (Fig. 1b). Further west, the deformation becomes more diffuse with highly distributed faulting, so that it is no longer possible to distinguish independent MNAF and SNAF strands among this southern NAF zone.

The MNAF has been traditionally divided into three major sections over a total length of 135 km (Barka and Kadinsky-Cade, 1988; Fig. 3). (1) Between the Gulf of Gemlik and Iznik Lake, the fault shows a roughly E-W direction (segment A), until a 12 km long releasing bend around Sölöz delta, southwest of the Lake. (2) The fault follows the southern coast of Iznik Lake with an E-W orientation (segment C), and continues in the narrow valley of the Kirandere with a constant azimuth of ~80°. This section in the west of Iznik Lake is marked by greater structural complexity and distribution of the deformation across several overlapping faults (segments D and E). Öztürk et al. (2009) suggested the existence of a continuous strike-slip fault extending along the deepest area of Iznik Lake, while Gastineau et al. (2021) evidenced an active fault strand following the northeastern edge of the lake's southern sub-basin, in a pull-apart configuration (Fig. 3b). East of Iznik Lake, Sipahioglu and

Matsuda (1986) reported the presence of two lineaments in this section: a geological boundary fault with no marker of Quaternary activation, and an active fault strand crosscutting and deforming recent alluvium. The eastern end of this section around the town of Mekece consists in a narrow, 1 km wide releasing step-over. (3) East of the step-over, the MNAF borders the south of the Geyve-Pamukova basin with a 70-80°N strike (segments F and G). The fault is associated to another fluvial system with the Sakarya River, collecting waters from the Anatolian plateau to the Black Sea. The river itself presents a large-scale right-lateral offset across the fault, estimated around 15-20 km (Fig. 3; Koçyigit, 1988; Özalp et al., 2013). The eastern edge of the basin is marked by a short restraining bend, after which the fault continues with a similar strike in the mountainous area of Akyazi where it connects to the main NAF (segment H).

3 Previous slip rates and paleoseismological studies on the MNAF

Geodetical horizontal slip rates along the MNAF of ~5±2 mm/yr were derived from strain accumulation modeling of fault-perpendicular GPS measurement profiles, despite a poor spatial distribution of the GPS sites (Ergintav et al., 2014; Straub et al., 1997). Meade et al. (2002) reported a similar estimate of 4.9±2.0 mm/yr for the segments east of Iznik using a GPS-based block modeling study. A more recent block modeling study estimated slip rates decreasing westward, and ranging between 4.2±1.3 mm/yr close to the MNAF-NAF junction and 3.1±1.5 mm/yr north of Manyas Lake (Fig. 2; Özbey et al., 2021). By comparison, the geodetic slip rate estimates along the NNAF in the Marmara region range at 20-25 mm/yr, with a lower horizontal rate of ~15 mm/yr in the Cinarcik basin south of Istanbul (Zabci, 2019).

The geological slip rates measured along the NNAF show lower values ranging at 15-20

mm/yr for the last 20 ka (Zabci, 2019). On the MNAF, a long-term horizontal slip rate was estimated by Gasperini et al. (2011) who used the displaced edge of a 11,250 years old submerged delta in Gemlik Bay to derive a 3.7±0.7 mm/yr minimal rate (Fig. 1b). This value was disputed by Vardar et al. (2014) who relied on a different offset value and an age of 30,000 years and derived a slip rate on the order of 2 mm/yr. Another value of 4.9±0.4 mm/yr was derived from the 16±1 km long offset of the Sakarya river in the Pamukova plain since the Late Pliocene (Özalp et al., 2013). The vertical motion was documented by Ikeda et al. (1991) who estimated a 0.7-1.4 mm/yr minimal rate from tilted post-glacial beachridges located on the western shore of Iznik Lake.
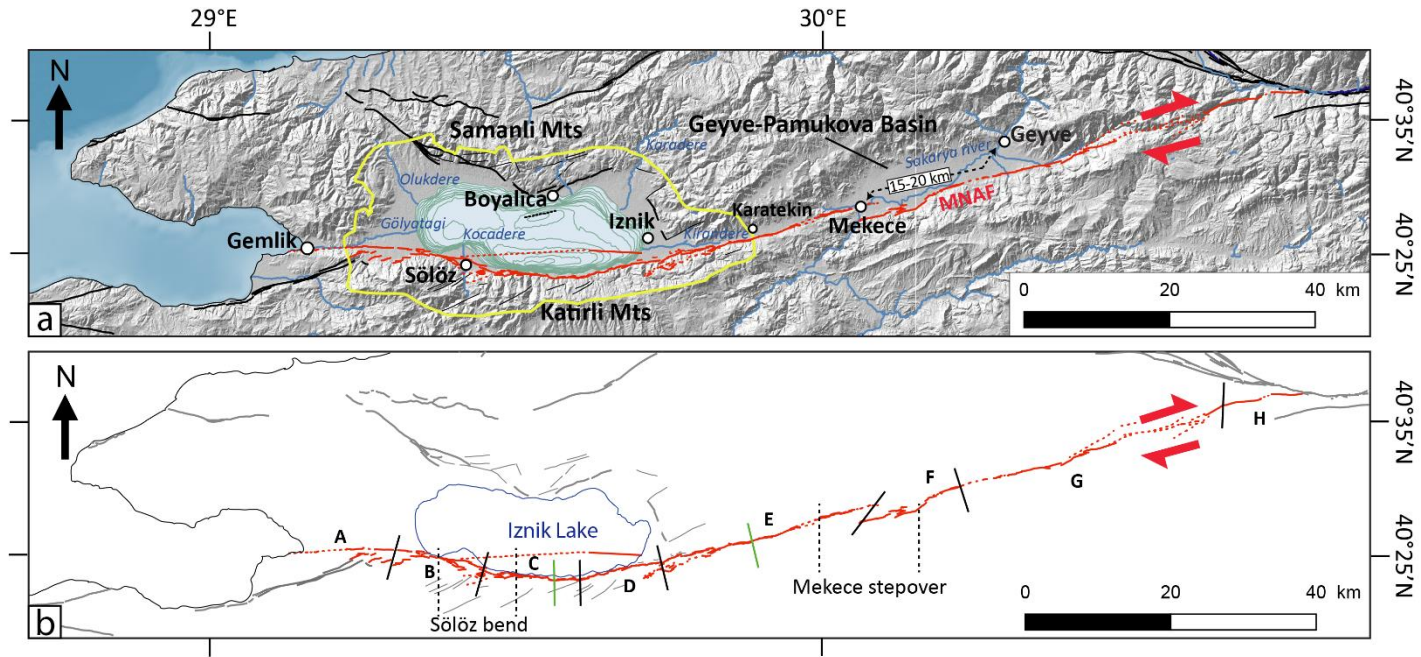
Figure 3. (a) General morphology of the eastern MNAF region. The footprint of the orthorectified Pleiades images (yellow) is superimposed on the Shuttle Radar Topography Mission (SRTM) model. The main rivers are drawn in blue. The MNAF is represented in red and the other active faults in black. Dotted lines indicate low confidence fault mapping (see section 4.2). The contours on the Iznik lake bottom are at a 5-meter interval (see Data Availability section). The fault traces within Iznik Lake are taken from Gastineau et al. (2021). (b) Segmentation of the main fault section analyzed in this study. Determined intersegments are located with black lines and alternative intersegments C/D et D/E with green lines (see section 4.3). Sölöz and Mekece step-overs' extent is shown with dashed lines.

1   A significant number of paleoseismological trenches have been dug along the MNAF (see e.g.

2   the syntheses of Akyuz & Zabci, 2012; Fraser et al., 2010) that led to the identification of several

3   ruptures during the last 4000 years (Fig. 2c). Yoshioka and Kusçu (1994) studied a site near

4   Geyve and identified a 3rd century BCE rupture and a later undated one. In the same area, an

5   unpublished trenching work by Akyüz et al. (2014) led to the identification of three presumed

6   earthquakes. In the east of Iznik, the last rupture was dated between the 13-14th and 18th centuries

7   CE (Honkura & Isikara, 1991; Ikeda, 1988). On the same segment, Barka (1993) opened nine

8   trenches and found three ruptures since ~2000 BCE, but none of them were dated precisely. In

9   the eastern part of Iznik Lake, Gastineau et al. (2021) evidenced a historical event in sediment

10 cores, that they correlated to the 1065 CE earthquake. South of the lake, Erginal et al. (2021)

11 reported a 50 cm high coseismic scarplet in beachrock deposits that they attributed to an 8th

12 century rupture. On the same segment, Civico et al. (2021) opened two trenches and evidenced

13 one mid-19th century event, one penultimate event after the late 7th century and two older events

14 before the mid-5th century CE. West of Iznik Lake, Ikeda et al. (1989) proposed a mid-19th

15 century event from archaeological remains found in a natural fault exposure. In Gemlik, Özalp et

16 al. (2013) found a similar age for the last event and dated the penultimate between the 12th and

17 18th centuries. So far, the largest trenching work has been conducted by Dogan (2010) who

18 opened 11 trenches on various MNAF segments. In many cases, very few or no age data could

19 be retrieved, which makes it difficult to discuss whether the identified ruptures are independent

20 from each other. Thus, in terms of earthquake recurrence, the paleoseismological data along the

21 MNAF remain largely inconclusive due to partial results or occasionally contradictory findings

22 (Fig. 2c).

23

24   **4 Fault geometry and segmentation analysis**

25   **4.1 Imagery datasets used**

26   Four stereo-pairs of Pleiades images covering the area between the Gulf of Gemlik, Iznik Lake,

27   and Karatekin (Fig. 3a) were processed to obtain a high-resolution DEM using the NASA Ames

28   Stereo Pipeline (ASP) software (Broxton and Edwards, 2008; Moratto et al., 2010; Shean et al.,

29   2016) without using ground control points (Fig. 4c,d). The original Pleiades images have a

30   resolution of about 50 cm, while the derived DEM has a horizontal resolution of 2 m and an

31   absolute vertical precision better than 10 m. The DEM was then used to orthorectify the original

32   optical images with the same ASP software. For the area east of 29.88E, which was not covered

33   by our Pleiades images, we relied on Google Earth images (Pleiades images from CNES/Airbus,

34   and QuickBird and WorldView images from Maxar Technologies), the SRTM elevation model

35   and the active fault map of Emre et al. (2011).

36   **4.2 Fault mapping and along-strike geomorphology**

37   The trace of the MNAF between Karsak pass and Akyazi was mapped using the satellite imagery

38   described in the previous section and complementary observations gathered in the field (Fig. 2a,

39   4). In the area benefiting from Pleiades coverage, secondary faults north and east of Iznik Lake

40   were also mapped (Fig. 3). To locate the fault trace, we especially relied on high confidence

41   geomorphological features, such as series of horizontally offset gullies and ridges, shutter ridges,

42   well-defined scarps and facets. Along some other sections, particularly those lacking multiple

43   consistent offsets, the mapping relied on lower confidence features, including large scale

44   lineaments and slope breaks (Fig. 4).
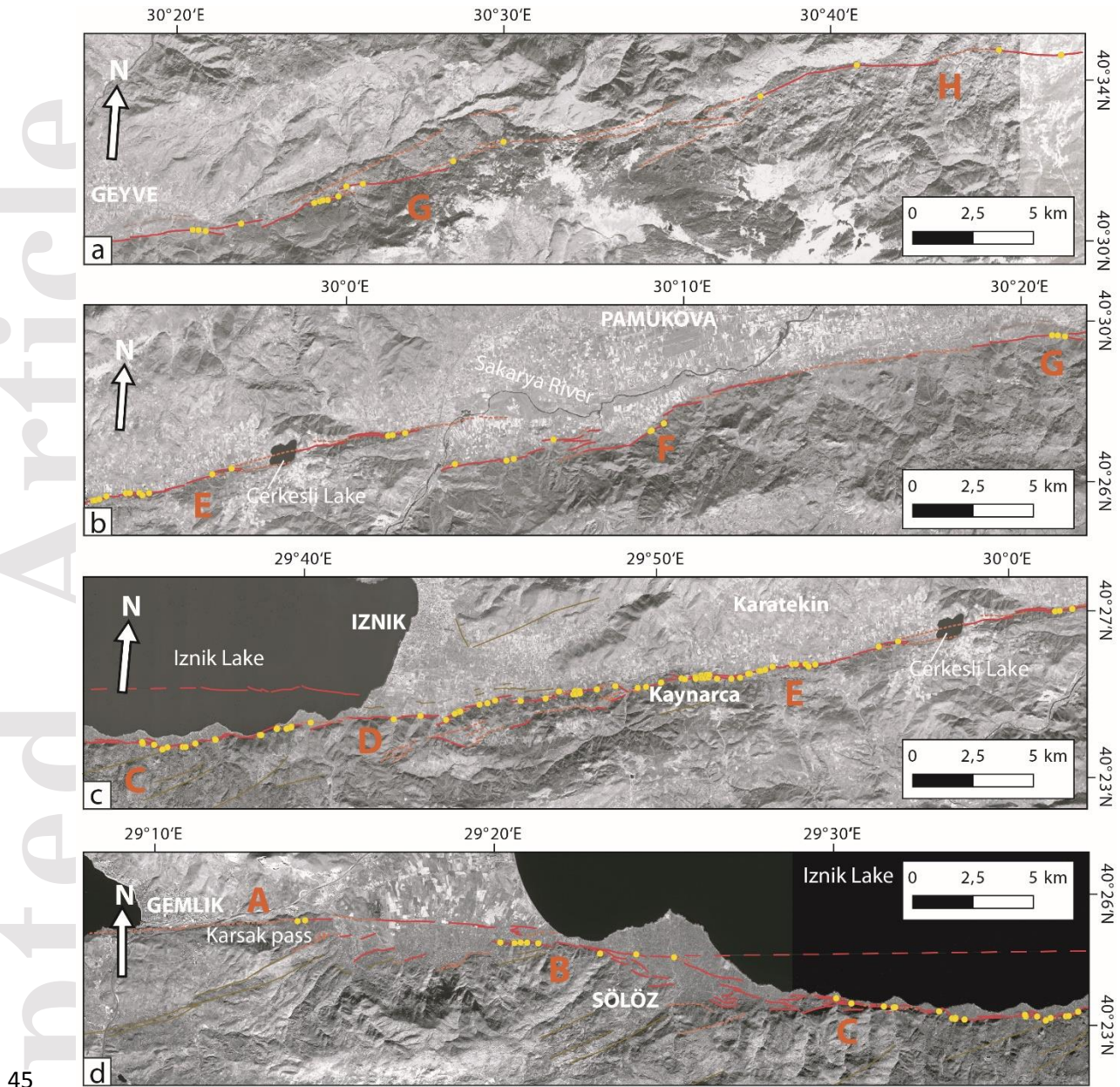
Figure 4. Surface trace of the eastern MNAF, superimposed on the Pleiades orthorectified images around Iznik Lake and Sentinel 2 images (Copernicus Sentinel Data [2018]) in other areas. Solid thick, dotted, and thin red lines refer to high confidence, low confidence, and secondary fault mapping, respectively. Other active faults are drawn in green. The subaqueous fault trace is taken from Gastineau et al. (2021). The yellow dots locate the markers associated with the offsets measured. The areas (a to d) are presented from east to west. Our proposed

52   segmentation (A to H) is also displayed.

53   Evidence for late Quaternary deformation can be observed in the landscape along the MNAF

54   segments between the Gulf of Gemlik and Akyazi district (Fig. 2a, 3, 4). East of the Gulf of

55   Gemlik, a small, E-W trending fault scarp borders the south of Gemlik alluvial plain and runs

56   along the narrow Karsak pass (Fig. 4d). East of Karsak pass, several parallel faults stretch

57   between the Eocene sedimentary rocks of the mountain range and the derived wide alluvial fan

58   south of the Gölyatagi stream (Fig. 3a, 4d). Southwest of Iznik Lake, a set of overlapping and en

59   echelon fault scarps are visible between the basement rocks and the Holocene alluvium of the

60   large Sölöz delta, striking WNW-ESE. However, the horizontally offset markers are found along

61   an E-W fault strand crossing the delta and forming a releasing bend with the fault section

62   running south of the lake.

63   East of the delta, the fault shows again an E-W orientation with a succession of short, en echelon,

64   recent scarps in the narrow coastal plain south of the lake (Fig. 4c, d). The association of several

65   laterally offset gullies and vertical, south-facing scarplets (Fig. S1 and S2c) evidences the recent

66   dextral motion across the fault with a normal component. A series of significant triangular facets

67   have developed in the same section along the north-facing side of the Katirli range (Fig. 3a),

68   which suggests long-term cumulative normal deformation in addition to the strike-slip tectonics.

69   Southeast of the lake, the fault becomes more oblique to the main NAF direction, striking 80-

70   85°N (Fig. 4c). East of Iznik Lake, the fault follows the southern edge of a 15 km long narrow,

71   linear valley with a more continuous, simpler and straight trace (Fig. 4c). Between Iznik and

72   Kaynarca, large-scale lineaments mark an oblique branch extending south of the main fault zone

73   and striking 70°N. On the main fault line, markers of strike-slip deformation, such as shutter

74   ridges, offset drainages and alluvial fan surfaces, are well developed (Fig. S2b). Occasionally,

75   parallel or en echelon successive faults can be traced in the landscape. This is the case between

76   Kaynarca and Karatekin where secondary branching can be traced through a series of fan

77   surfaces showing several offsets (Fig. 4c). This geometrical complexity is associated with an

78   orientation change to 80°N. Close to Mekece, a series of laterally displaced streams running

79   along a north facing scarp show cumulative dextral offsets ranging between 10 m and 25 m.

80   Further east, the fault crosses the Sakarya river and forms a ~1 km wide releasing step-over (Fig.

81   4b). The eastern section of the stepover is composed of shorter, en echelon faults. The fault then

82   follows the southern edge of the Geyve-Pamukova basin as a single, simple straight trace with a

83   70-80°N, but is associated with fewer markers of Holocene horizontal deformation. East of the

84   Geyve plain, the fault runs in the middle of a mountainous area and the precise mapping of the

85   junction with the main NAF strand is less certain (Fig. 4a).

86

4.3 Fault segmentation

88   To properly interpret the set of deformed markers observed along the fault, it is needed to first

89   determine the fault segmentation. Such segmentation can also provide first-order constraints on

90   the maximum length and magnitude of earthquake that can be expected. The kind of boundary

91   between the successive segments (azimuth difference, width and length of the step-overs. . .) is

92   also thought to control whether a given rupture is likely to propagate through several segments

93   (Aki, 1984; Barka & Kadinsky-Cade, 1988; Wesnousky, 2006). We decomposed the eastern

94   MNAF zone into several successive segments using the automatic procedure developed by

95   Klinger (2010). The digitized MNAF trace was first simplified and resampled each 50 m. The

96   numerical method models the fault as a continuous set of linear segments and seeks, for a given

97   number of segments, the distributions of segment boundaries which best approximate the actual

98   fault trace, using a l_1 trend filtering method (Kim et al., 2009). The brutal increase in the curve of

99   the RMS-misfit as a function of the number of segments indicates that a minimal range between

100   8 and 19 segments is needed to describe the fault trace with a good trade-off between data-model

101   misfit and limited number of segments (Fig. S3). We especially explored this space of solutions

102   and found that the locations of most frequently selected inter-segments for this range cluster on

103   12 points of the fault. Keeping the solutions that included the most visible geometrical

104   discontinuities along strike (e.g. Sölöz and Mekece stepovers, kinks at 29°35'E and south of

105   Iznik) led us to favor a decomposition of the MNAF into 8 segments (denoted A to H on Fig.

106   3b).

107   Overall, the boundaries most frequently selected correspond to the major strike change occurring

108   south of Iznik Lake (C/D inter-segment, Fig. 3b) and the releasing bend at the eastern edge of the

109   Geyve-Pamukova basin (G-H inter-segment). The significant discontinuities of Sölöz bend (B/C

110   inter-segment) and Mekece stepover (E/F inter-segment) also correspond to recurrently selected

111   boundaries. Some other chosen boundaries are less recurrent. The D/E inter-segment is

112   associated with a minor variation in azimuth but also with a more visible change from multiple

113   parallel branches to a single, simpler fault trace eastward. The F/G inter-segment also reflects a

114   transition from small en echelon faults to a single linear fault line eastward.

115

116   **5 Cumulative and coseismic offsets**

117   **5.1 Method of measurement and uncertainties**

118   Major ground rupturing earthquakes generate meter-scale deformations that can be preserved in

119   the morphology through several seismic cycles (e. g. Ansberque et al., 2016; Klinger et al., 2011;

120   Kurtz et al., 2018). In the case of strike-slip ruptures, it is generally possible to measure in the

121   days following the earthquake a series of laterally displaced markers such as roads, fences, walls,

122   field or vegetation lines, terrace risers or gullies (Rockwell et al., 2002). Older morphological

123   markers can also show larger, cumulative values of offset representing the summation of several

124   coseismic displacements. If enough markers of various ages are preserved along the fault, the

125   compilation of a large number of offset measurements is expected to give several clusters of

126   values, corresponding to the cumulative displacement for various numbers of earthquakes

127   (Beauprêtre et al., 2012, 2013). The offset measurements carried out after recent earthquakes

128   have evidenced that the coseismic slip located on the fault often shows significant variations

129   along-strike, as high as 30-40% around the mean displacement (Choi et al., 2018; Lin et al.,

130   2020; Reitman et al., 2019; Rockwell et al., 2002; Zielke, 2018). The off-fault deformation,

131   which is difficult to measure during post-seismic surveys, can also be significant (Antoine et al.,

132   2021; Choi et al., 2018; Rockwell et al., 2002). Despite the erosive and sedimentary processes

133   which tend to erase the smallest coseismic offsets, the measurement of cumulative offsets can

134   also give access to this slip variability on longer time scales (Rizza et al., 2011).

135

	Total	Segment A	Segment B	Segment C	Segment D	Segment E	Segment F	Segment G	Segment H
Length (full mapping, km)	148	14.4	12.5	13.9	11.5	31.2	16.4	36.6	11.5
Length (confident mapping, km)	107	4.1	12.5	13.6	11.1	24.1	14.9	17.3	9.2
Number of measurements	114	2	10	14	15	50	7	12	4
Measured on Pleiades topography	45	1	6	8	8	22	0	0	0
% Pleiades topography	39	50	60	57	53	44	0	0	0
Measured on Pleiades image	32	1	4	6	7	14	0	0	0
% Pleiades image	28	50	40	43	47	28	0	0	0
Measured on Google Earth image	37	0	0	0	0	14	7	12	4
% Google Earth image	32	0	0	0	0	28	100	100	100
Mean quality /20	12	14	12	11.1	12.3	12.3	10.7	11.8	12.3
Density of data per km	0.77	0.14	0.80	1.01	1.30	1.60	0.43	0.33	0.35
Density of data (confident mapping)	1.07	0.49	0.80	1.03	1.35	2.07	0.47	0.69	0.43
Number of COPD peaks (2σ model)			5	7	11	8	4	6	
Number of COPD peaks (1σ model)			4	4	5	8	4	4	2

136

137   **Table 1.** Summary of the main characteristics of the fault mapping and offset measurements datasets used in this study.

138

139

140   Along a 148-km long portion of the eastern MNAF, we identified and systematically

141   measured 114 offsets (Tables 1 and S3, see Data Availability section). 40% of the

142   measurements were performed using Pleiades topographic data, while Pleiades ortho-rectified

143   images and Google Earth images each represent 30% of the measurements. The displaced

144   markers considered are river channels, gullies, terrace risers and more occasionally vegetation

145   lines and ridges. We favored markers making a high angle with the fault in order to minimize

146   the apparent offset linked to unaccounted-for vertical slip. For each marker, we define

147   piercing lines, i.e. points that were aligned before the displacement, and that we project on the

148   fault trace. The piercing points across the fault are then realigned by retro-deformation, which

149   gives the offset value (Fig. 5). When one marker is displaced by several parallel fault strands,

150   the offset value to be considered is the sum of the measurements on each fault line (Zielke et

151   al., 2015). Five offsets were also measured in the field with tape (Fig. 6). One field

152   measurement (marker 153) ranges significantly lower than the Pleiades measurement due to

153   different reconstruction hypothesis. The other field measurements are in general in fair

154   agreement with the values obtained from satellite imagery, though ~10% lower on average.

155   The relative underestimation of field offset measurements compared to satellite imagery has

156   been noticed in previous studies (see another example in Klinger et al., 2005) suggesting that

157   the distributed deformation is better assessed in the latter case (Antoine et al., 2021).

158

159

160
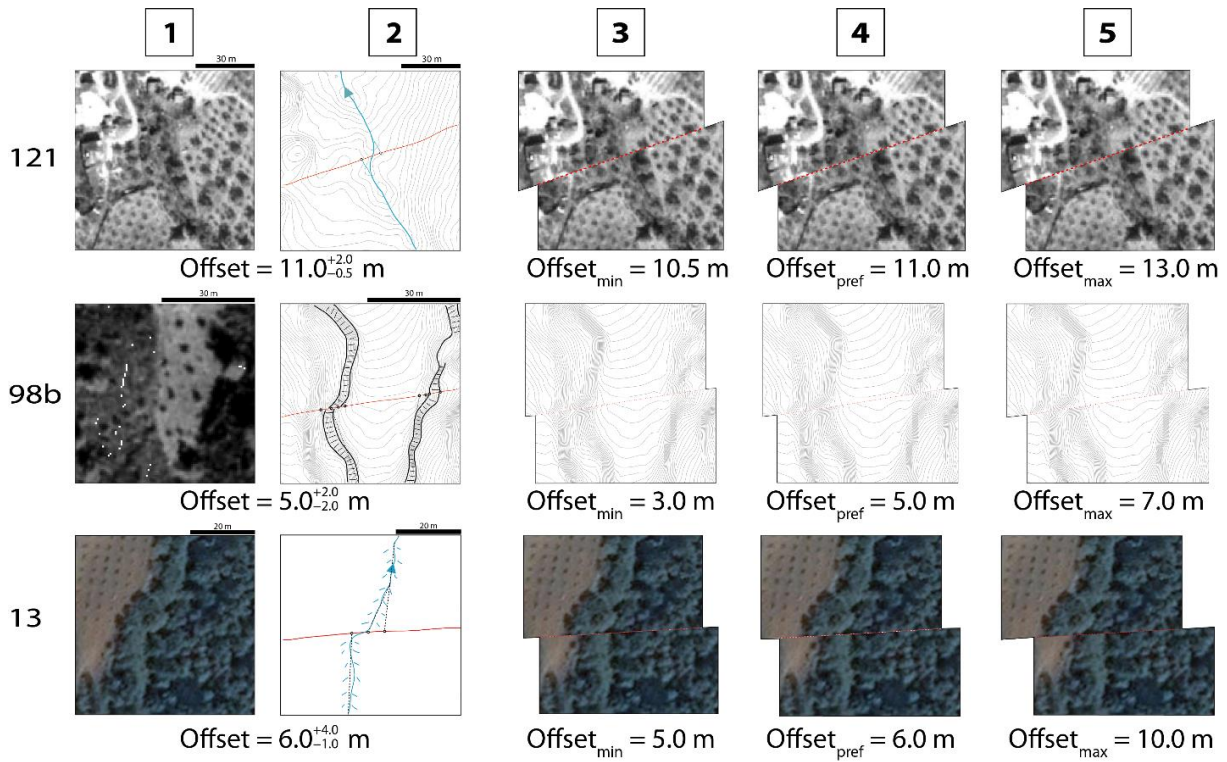
Figure 5. Examples of horizontal offset measurements. Marker ID code is indicated on the left. North direction is upward. From top to bottom, measurements were respectively done using the Pleiades image, topography, and the Google Earth image. Columns 1 and 2 show the original morphologies. The fault is drawn in red. Black lines and circles refer to the piercing lines and points. Columns 3, 4 and 5 show the retro-deformed morphologies giving the minimum, preferred and maximum offset values respectively. For the full dataset, see Data Availability section.

172
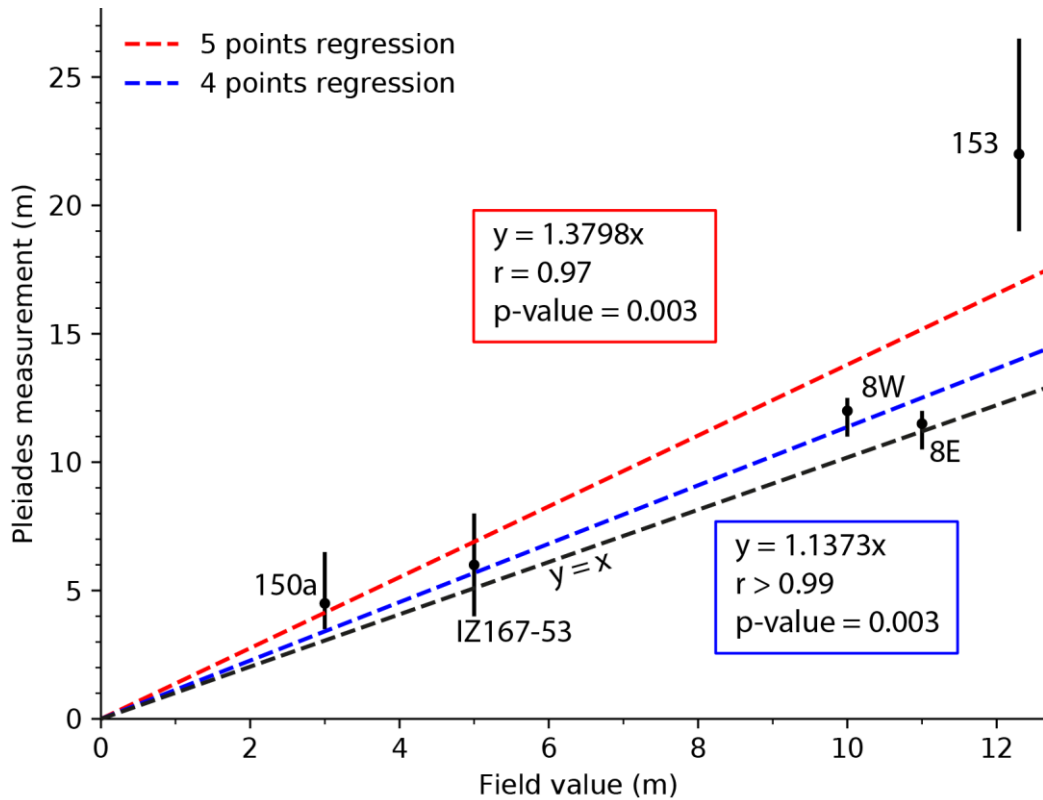
Figure 6. Comparison between field and Pleiades offset measurements. Two linear

regressions are shown, including all data points (red) and excluding marker 153 (blue). For

each regression we present the equation, Pearson's correlation coefficient *r* and the p-value.

176

The uncertainty of the offset measurement mainly originates from the various possibilities for

interpreting and restoring the original, non-deformed geometry of the marker (Ansberque et

al., 2016; Manighetti et al., 2015). Therefore, each measurement consists in our preferred

value for the best reconstruction, and a minimum and a maximum value, each representing an

extreme plausible reconstruction. We use conservative min/max reconstructions, larger than

±15% of the preferred value on average, so that there is only a small probability that the real

offset falls out of this range (Gold et al., 2013). Each measurement is given a 20-points

quality score, which reflects the intrinsic quality of each marker in providing a relevant

measure (Beauprêtre et al., 2013; Choi et al., 2018; Kurtz et al., 2018; Zielke et al., 2012).

186 This score includes the following criteria: (a) confidence that the offset marker is of tectonic

187 nature and weakly man-modified, (b) degree of preservation (marker visibility and sharpness),

188 (c) marker shape (width and sinuosity), (d) fault zone complexity (plausible fault zone width

189 and number of fault splays), (e) angle of marker with fault, (f) resolution of used dataset (a

190 detailed explanation of how the quality score is determined can be found in Supporting

191 Information).

5.2 Statistical analysis

193 The 114 offsets measured range between 2.5 and 64 m, with a majority of values smaller than

194 30 m (Fig. 7b, Table S3). In order to identify the most significant offset clusters along each

195 fault segment, which could represent the cumulative signature of past ruptures, we represent

196 the offset values as probability density functions (e.g. Beauprêtre et al., 2012; Kurtz et al.,

197 2018; McGill and Sieh, 1991; Zielke et al., 2010). Each offset measurement is represented

198 with an asymmetric Gaussian distribution, the preferred measured value being the peak of the

199 Gaussian probability density function (PDF). Since the minimum and maximum offsets

200 reflect geologically plausible bounds for the reconstruction values and do not directly

201 correspond to real standard variations (Scharer et al., 2014), we compare two models where

202 these maximum and minimum ranges are taken as $\pm 1\sigma$ and $\pm 2\sigma$ half-widths of the PDF

203 (referred hereafter as "1σ model" and "2σ model").

204

205
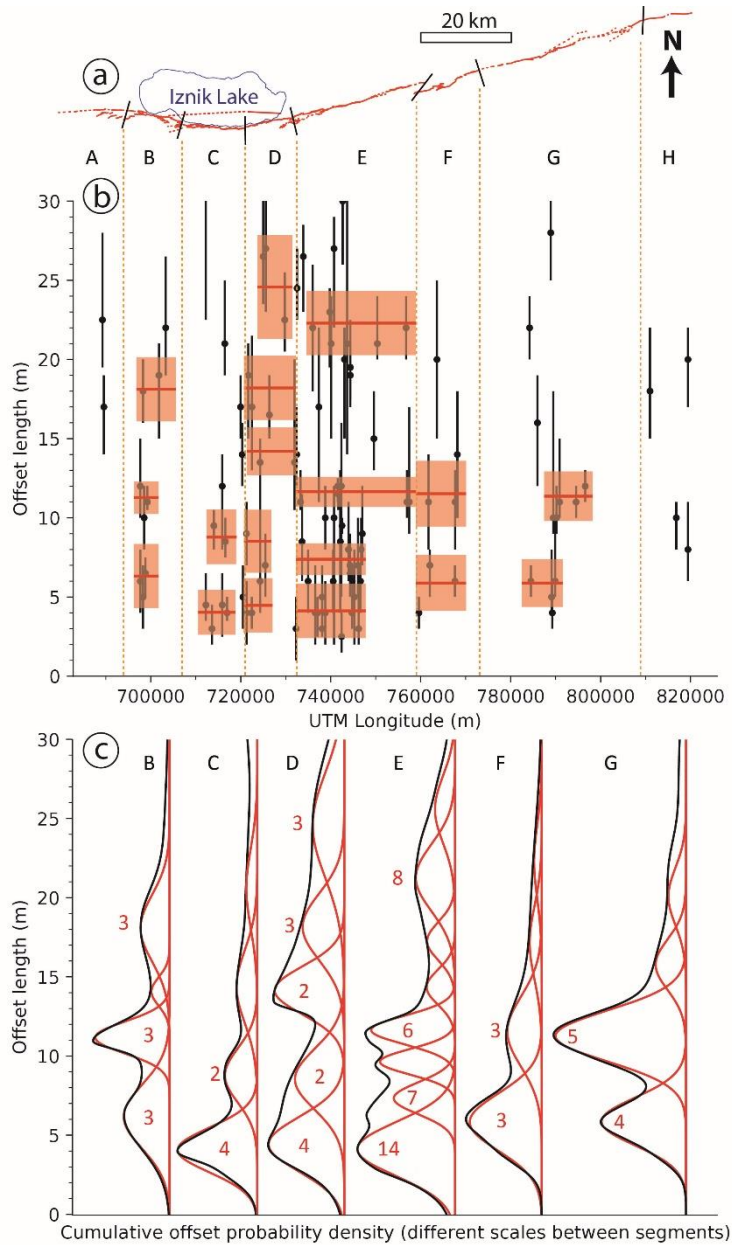
Figure 7. (a) Map of the fault section studied with our proposed segmentation. (b) Horizontal

offsets measured along the fault in the range 0-30 m. The color boxes represent the best

constrained peak values, within 1σ uncertainties, obtained on the cumulative offset probability

distribution (COPD) curves for each segment. The segments are separated by the vertical

orange broken lines. (c) COPD curves (black lines) and modeled average slips (red lines) for

the 1σ model. The number of supporting individual measurements is indicated for the best

constrained COPD peaks.

214   The individual PDFs for each segment are then summed into a cumulative offset probability

215   distribution (COPD) curve, using the quality scores as weights for each individual offset

216   measurement (Fig. 7c and 8a). The COPD generally presents local peak values, which indicate

217   the most frequent offsets measured along the fault section considered. The contribution of each

218   measurement in the shape of the COPD depends both on its uncertainty and on its quality score.

219   A larger uncertainty corresponds to a wider and flatter individual PDF, which consequently

220   contributes less to define a clear COPD peak. A lower quality score decreases the effect of the

221   measurement in changing the shape of the COPD. For each COPD curve, it is assumed that the

222   value associated to the first peak value corresponds to the offset related to the most recent large

223   earthquake preserved along that specific segment. The average slip associated with this last

224   rupture is empirically extracted from the COPD through several steps (Kurtz et al., 2018). (1)

225   The rising part of the COPD curve is used to build a symmetric Gaussian function, which

226   represents the modeled average slip associated to the most recent rupture along the segment

227   considered. (2) This modeled function is subtracted from the COPD to derive a residual COPD

228   (Fig. 8b). This residual curve is assumed to represent the cumulative tectonic deformation

229   recorded in the landscape before the most recent earthquake occurred. (3) In general, the rising

230   part of the COPD does not strictly follow a Gaussian function, which produces a residual

231   negative artefact located ahead of the following peak values. This residual is discarded by

232   resetting all negative values to zero before the next extraction. As these steps are iterated (Fig.

233   8c), the residual COPD curve flattens and the Gaussian fit becomes less constrained. To avoid

234   extracting artifacts which are not supported by measurements, the peaks with an amplitude below

235   10% of the maximum amplitude of the original COPD are judged unreliable and are discarded

236   (following Kurtz et al., 2018). The iterations are stopped when no additional peak can be

237   constrained.

238   The validity of this method for extracting peaks and interpreting them as slip signals relies on

239   several assumptions. The resolution of satellite imagery and the uncertainties of offset

240   measurements limit the detection of small slip signals. In our case, this minimum detectable slip

241   ranges at ~2.5 m, which implies we cannot detect events of Mw below 7. We assume that the

242   variability of coseismic slip over short distances along strike is limited enough to produce

243   relevant clusters of offset measurements. It is also assumed that these measurements result from

244   predominantly intermittent and seismogenic slip with negligible contributions of creep, slow slip

245   or afterslip. The production of geomorphic markers must happen more frequently than the large

246   earthquakes for the geomorphic slip record to be complete. The production of these markers is

247   also assumed to be stable over the time window considered. These assumptions will be addressed

248   together with the discussion of the results.

249   Interpreting COPD peaks as individual slip signals must be done with caution, especially when

250   relative measurement uncertainties are high and when only few data points are available along a

251   segment. Because of the natural variability in coseismic slip along strike, offset measurements

252   from a single event can produce bimodal distributions (Lin et al., 2020; McGill & Rubin, 1999).

253   Conversely, one large increment might hide two separate, smaller events, but undistinguished

254   due to too few data and/or too large individual uncertainties (e. g. Liu-Zeng et al., 2006; Zielke et

255   al., 2010). Once the COPD peaks are extracted for a given segment, we assess the statistical

256   significance of each peak by looking at the following criteria (Tables 2 and 3): number of

257   supporting individual measurements, spreading of the data supporting the first two peaks, degree

258   of overlapping with preceding peak, sensitivity to alternative segmentation (for segments C, D,

259   E).
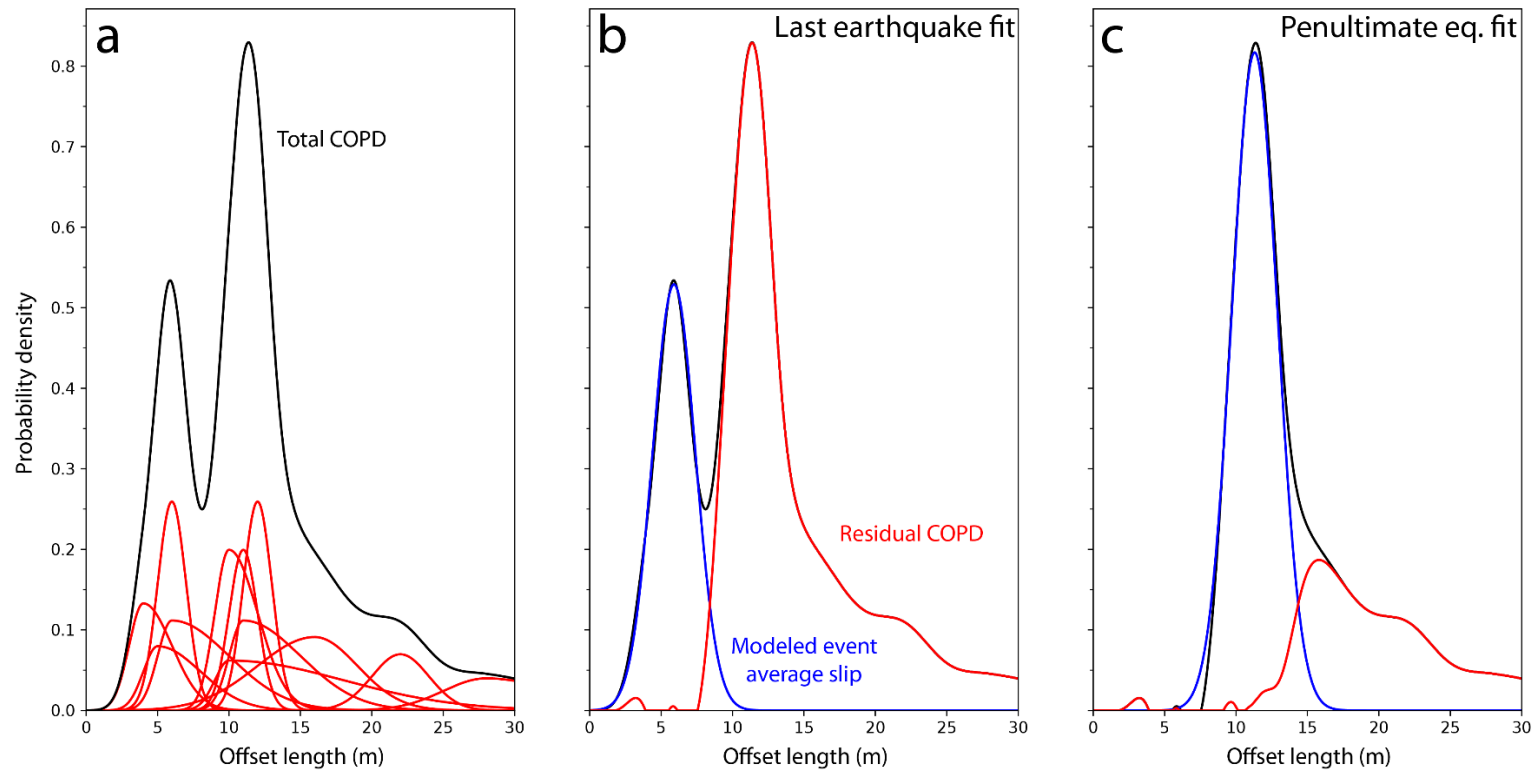
Figure 8. Illustration of the statistical analysis methodology used for the offset measurements of segment G. (a) Probability density functions of the individual measurements (in red) and corresponding Cumulative Offset Probability Density (COPD, in black). (b) Modeling of the last major surface rupture signal by fitting the increasing part of the COPD with a Gaussian curve (in blue). The red line is the residue of the COPD after subtracting this last rupture slip model. (c) Same process as (b) for the presumed penultimate event.

5.3 Results

Tables 2 and 3 present the offset values extracted from the COPD peaks for each fault segment in the range 0-30 m. We extracted between 4 and 11 peaks per segment for the 2σ model and between 4 and 8 peaks for the 1σ model (Table 1). Smaller modeled uncertainties tend to increase the number of extracted peaks per segment. This effect is most significant for segment D where the number of peaks for the 2σ model is two times larger. However, most of the extracted peaks for the 2σ model show poor statistical robustness. Half of them are not supported by more than one individual measurement (Table 3). For some of them, the increment with the preceding peak is not significantly different from zero. Several of them do not pass the segmentation test. This likely results from a high degree of data scattering compared to uncertainties, especially for segments with small numbers of measurements. Segment E does not show this feature because of its high spatial density of measurements, which is more than twice as high as the average density of the other segments (Table 1).

To check for potential biases resulting from this higher density of measurements, we performed a supplementary test on segment E. We produced and analyzed five random subsets of 18 measurements obtained on segment E, so that the measurement density of the subsets equals the average density of the other segments, i.e. 0.75 measurement per km. We then identified which extracted peaks remained consistent between all subsets. The sensitivity tests for that segment suggest that only the first two peaks are statistically robust. These peaks still present a high degree of overlapping.

Most peaks obtained with the 1σ model are statistically stronger than those obtained with the 2σ model (Table 2). When only the more robust peaks are considered, both models show similar

287   results (Table 4, Fig. 7b). Segments A and H did not provide statistically significant peaks due to

288   the very small number of measurements.

289   We identified two to five statistically robust cumulative slip increments for segments B to G,

290   ranging between 4 and 25 m. Offset values show consistency between all segments for the first

291   two extracted peaks at ~5 and ~10 m. However, the central segments C, D and E show lower

292   mean values of increments, from 3.2 m to 4.7 m, while they range between 5 and 6.2 m on

293   segments B, F and G. On segment E, despite the higher density of measurements, the events are

294   harder to separate and their respective displacement is less constrained due to the larger

295   scattering of data points. Peak values differ more for higher peaks (Table 4).

Segment	Mean value	(±1σ)	Increment with preceding peak	(±1σ)	Number of supporting measurements	Mean quality	Spreading with previous peak	Overlapping coefficient with previous peak	Sensitivity to segmentation	Sensitivity to downsampling
B	6.2	2			3	12.7				
B	11.2	1	5	3	3	12	<30%	0.09		
B	14.1	0.9	2.9	1.9	0			0.13		
B	18.1	2.1	4	3	3	12		0.16		
C	4.1	1.4			4	14.3				
C	8.8	1.7	4.7	3.1	2	11	<30%	0.13		
C	14.4	2.3	5.6	4	3	9		0.16	x	
C	20.6	2.5	6.2	4.8	1	11		0.2		
D	4.5	1.7			4	12.3				
D	8.6	1.9	4.1	3.6	2	10	<30%	0.25		
D	14.2	1.5	5.6	3.4	2	14.5		0.1		
D	18.2	2.1	4	3.6	3	14		0.26		
D	24.6	3.3	6.4	5.4	3	11.3		0.23		
E	4.2	1.7			14	12.8				
E	7.4	1	3.2	2.7	7	12.1	<30%	0.23		
E	9.7	0.8	2.3	1.8	4	10.8		0.2		x
E	11.7	0.9	2	1.7	6	13.3		0.24		
E	14.4	1.1	2.7	2	2	11		0.18		x
E	17.3	1.2	2.9	2.3	2	13		0.21	x	x
E	21.3	2.1	4	3.3	8	11.6		0.21		
E	25.6	2.1	4.3	4.2	3	13.7		0.31	x	x
F	5.9	1.8			3	10.7				
F	11.6	2.2	5.7	4	3	10	<30%	0.15		
F	17.2	2.3	5.6	4.5	0			0.21		
F	22.3	2.3	5.1	4.6	1	13		0.27		
G	5.9	1.5			4	11.3				

Segment	Mean value	(±1σ)	Increment with preceding peak	(±1σ)	Number of supporting measurements	Mean quality	Spreading with previous peak	Overlapping coefficient with previous peak	Sensitivity to segmentation	Sensitivity to downsampling
G	11.3	1.6	5.4	3.1	5	13.2	<30%	0.08		
G	15.8	1.6	4.5	3.2	1	16		0.16		
G	20.1	1.8	4.3	3.4	1	7		0.21		
H	9.4	2			2	13				
H	18.7	2.7	9.3	4.7	2	11.5	30-40%	0.05		

296 **Table 2.** COPD peaks extracted for the 1σ model. Mean quality is computed on the set of individual measurements supporting each

297 peak. Spreading value is expressed in % of the mean of measurements supporting the first two peaks per segment. The overlapping

298 coefficient is computed using normalized distributions.

Segment	Mean value	(±1σ)	Increment with preceding peak	(±1σ)	Number of supporting measurements	Mean quality	Spreading with previous peak	Overlapping coefficient with previous peak	Sensitivity to segmentation	Sensitivity to downsampling
B	6.1	1.3			3	12.7				
B	9.9	0.6	3.8	1.9	1	13	<30%	0.04		
B	11.1	0.4	1.2	1	1	15		0.22		
B	12.3	0.9	1.2	1.3	1	8		0.32		
B	18.2	1.4	5.9	2.3	2	13.5		0.01		
C	3	0.5			1	17				
C	4.2	0.5	1.2	1	3	13.3	>40%	0.23		
C	5.4	0.5	1.2	1	0			0.23		
C	9	0.8	3.6	1.3	3	10	<30%	0.05		
C	13.9	1.6	4.9	2.4	1	11		0.04	x	
C	17.2	0.7	3.3	2.3	1	8		0.14	x	
C	21.2	1.6	4	2.3	1	11		0.07		
D	4.2	0.8			3	14				
D	6.8	1	2.6	1.8	2	6.5	30-40%	0.15		

D	9	1	2.2	2	1	14	<30%	0.27		
D	13.2	1.9	4.2	2.9	0			0.14	x	
D	13.7	0.5	0.5	2.4	2	14.5		0.42		
D	14.9	0.5	1.2	1	0			0.23		
D	16.6	0.7	1.7	1.2	2	15		0.15		
D	18.2	0.9	1.6	1.6	1	12		0.31	x	
D	19.8	0.6	1.6	1.5	1	12		0.26		
D	22.5	1.2	2.7	1.8	1	14		0.16	x	
D	26.5	1.7	4	2.9	2	10		0.16		
E	3.8	1			10	13				
E	6.4	0.9	2.6	1.9	7	11.3	<30%	0.17		
E	8.3	0.6	1.9	1.5	4	13.8		0.2		x
E	9.6	0.5	1.3	1.1	4	10.8		0.24		x
E	11.4	0.7	1.8	1.2	6	13.3		0.13	x	x
E	14.4	1.5	3	2.2	3	11.7		0.16	x	x
E	19.7	1.7	5.3	3.2	6	12.8		0.1		x
E	24	2.6	4.3	4.3	5	11.4		0.31	x	
F	4	0.5			1	9				
F	6.2	0.8	2.2	1.3	2	11.5	>40%	0.09		
F	11.1	1.5	4.9	2.3	3	10	<30%	0.03		
F	19.6	3	8.5	4.5	1	13		0.06		
G	4.1	0.6			2	9				
G	6	0.7	1.9	1.3	2	13.5	>40%	0.14		
G	8	0.5	2	1.2	0			0.09		
G	11.3	1.2	3.3	1.7	5	13.2	<30%	0.05		
G	15.2	1.2	3.9	2.4	1	16		0.1		
G	22	1.1	6.8	2.3	1	7		0.003		

299

300 **Table 3.** COPD peaks extracted for the 2σ model. Mean quality is computed on the set of individual measurements supporting each

301 peak. Spreading value is expressed in % of the mean of measurements supporting the first two peaks per segment. The overlapping

302 coefficient is computed using normalized distributions.

303

304

305

306

307

308

309

310

311

312

	COPD peak values (m)					Increments between peaks (m)				
	Peak 1	Peak 2	Peak 3	Peak 4	Peak 5	Peak 1	Peak 2	Peak 3	Peak 4	Peak 5
B	**6.2±2** (6.1±1.3)	**11.2±1.0**	**18.1±2.1** (18.2±1.4)			**6.2±2** (6.1±1.3)	**5±3.0**	**6.9±3.1** (12.1±2.6)		
C	**4.1±1.4** (4.2±0.5)	**8.8±1.7** (9.0±0.8)				**4.1±1.4** (4.2±0.5)	**4.7±3.1** (4.8±1.3)			
D	**4.5±1.7** (5.5±1.8)	**8.6±1.9**	**14.2±1.5** (13.7±0.5)	**18.2±2.1** (16.6±0.7)	**24.6±3.3** (26.5±1.7)	**4.5±1.7** (5.5±1.8)	**4.1±3.6**	**5.6±3.4** (8.2±2.3)	**4.0±3.6** (2.9±1.2)	**6.4±5.4** (9.9±2.4)
E	**4.2±1.7** (3.8±1.0)	**7.4±1.0** (6.4±0.9)	**11.7±0.9**	**22.3±2.1**		**4.2±1.7** (3.8±1.0)	**3.2±2.7** (2.6±1.9)	**4.3±1.9**	**10.6±3.0**	
F	**5.9±1.8** (5.1±1.3)	**11.6±2.2** (11.1±1.5)				**5.9±1.8** (5.1±1.3)	**5.7±4.0** (6.0±2.8)			
G	**5.9±1.5** (5.1±1.3)	**11.3±1.6** (11.3±1.2)				**5.9±1.5** (5.1±1.3)	**5.4±3.1** (6.2±2.5)			

313

314 **Table 4.** Best constrained cumulative offsets and slip increments computed for each fault segment in the offset range 0-30 m. The

315 retained peaks respect the following conditions: significant increment with preceding peak, more than one supporting individual

316 measurement, less than 30% of spreading with previous peak, consistency through varying segmentation and downsampling.

317 Uncertainties are 1σ. Bold values are from the 1σ model. Values in brackets are those deduced from the 2σ model. We underline

318 values showing consistency between the two models.

319 **6 Terrace dating**

| Terrace	Sample code	Depth (cm)	Dissolved quartz mass (g)	^{9}Be carrier solution (g)	^{10}Be/^{9}Be ratio ± 1σ AMS uncertainty (10^{-15} blank corrected)	^{10}Be (10^4 at/g)	^{10}Be concentration uncertainty (%)	Sampling site location
T3	15TUR5-0a	0	17.179	0.2988	9.913 ± 1.208	1.1499	23.05	40.3974°N - 29.6966°E
T3	15TUR5-0b	0	18.480	0.2990	23.17± 6.328	2.5003	34.99	94±4 m asl
T3	15TUR5-20	20-35	2.864	0.3010	3.428 ± 0.744	2.4060	69.82	TS = 0.997
T3	15TUR5-60	60-70	10.739	0.2995	8.012 ± 0.956	1.4902	25.69	
T3	15TUR5-80	80-90	16.347	0.2980	12.25 ± 1.234	1.4896	17.91	
T3	15TUR5-130	130-140	6.789	0.2976	3.808 ± 0.556	1.1132	49.12	
T2	15TUR3-0a	0	20.549	0.3043	178.5 ± 6.176	17.6296	3.65	40.4963°N - 29.6813°E
T2	15TUR3-0b	0	18.510	0.3078	89.09 ± 5.310	9.8809	6.52	127±3 m asl
T2	15TUR3-60	60-85	20.824	0.2989	53.09 ± 4.953	5.0837	10.65	TS ~ 1
T2	15TUR3-110	110-130	19.941	0.2905	245.1 ± 8.848	23.8183	3.75	
T2	15TUR3-150	150-175	17.038	0.2993	200.4 ± 32.61	23.4781	16.79	
T1	15TUR4-0a	0	20.838	0.2979	226.9 ± 75.69	21.6293	34.27	40.5031°N - 29.6860°E
T1	15TUR4-0b	0	20.514	0.2973	313.7 ± 11.86	30.3225	3.89	164±3 m asl
T1	15TUR4-30	30-40	20.550	0.2958	255.4 ± 7.943	24.5165	3.24	TS ~ 1
T1	15TUR4-80	80-90	23.547	0.2981	292.6 ± 11.47	24.7008	4.03	
T1	15TUR4-130	130-140	20.510	0.2984	326.3 ± 10.80	31.6621	3.41	
T1	15TUR4-260	260-270	22.204	0.2966	184.8 ± 9.776	16.4640	5.52	
T1	15TUR4-370	370-380	20.771	0.2980	243.5 ± 12.71	23.2995	5.38	

320

321 **Table 5.** Characteristics of the terrace samples and results of the nuclide measurements. The ^{10}Be/^{9}Be ratio of the blank is $6.200.10^{-15}$
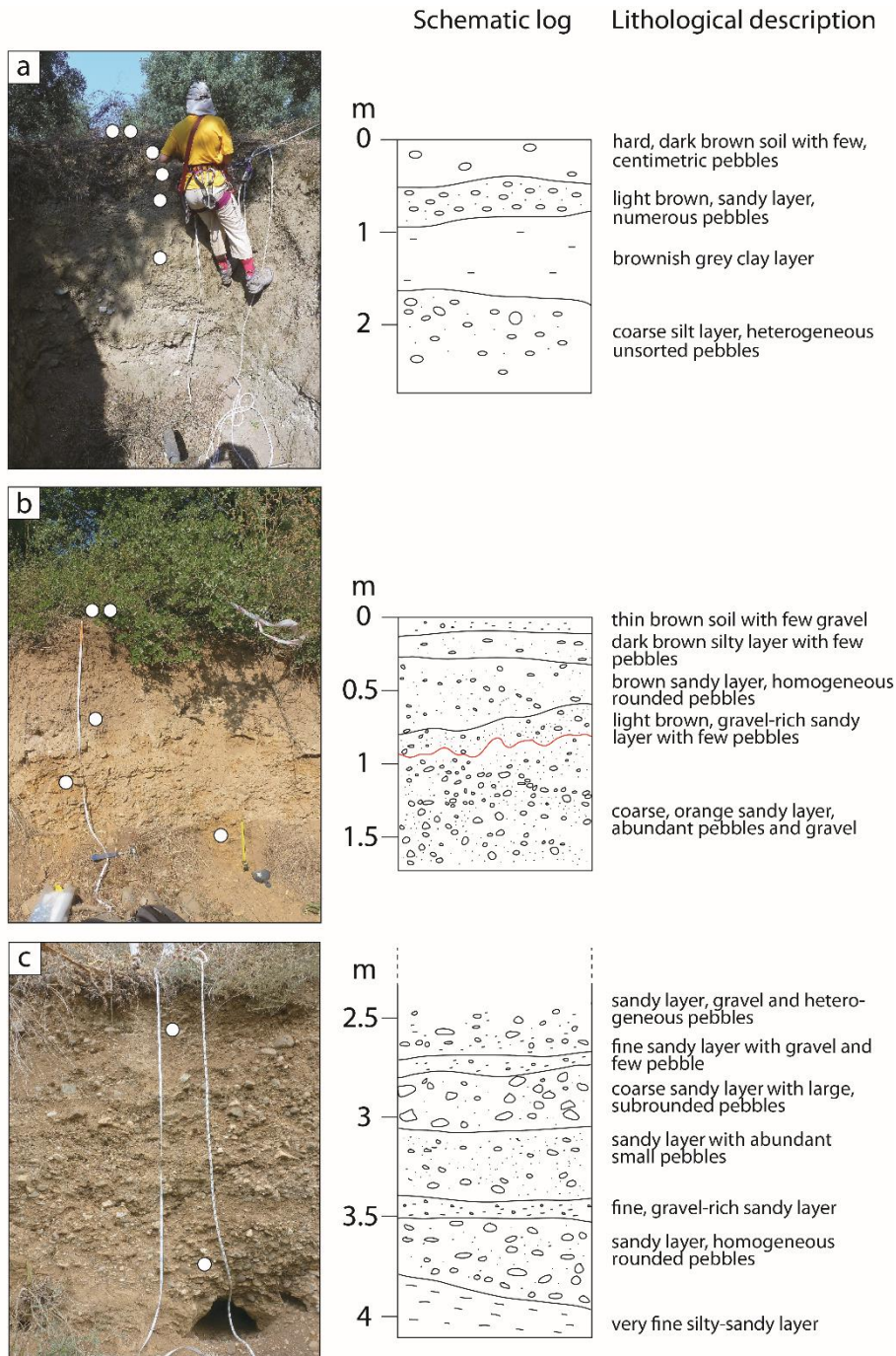
322 with an analytical uncertainty of 19%. TS is topographic shielding value. The total measurement error includes the uncertainties

323 associated with the AMS measurement, the blank value, the dissolved quartz mass and the spike mass weighing and concentration.

324
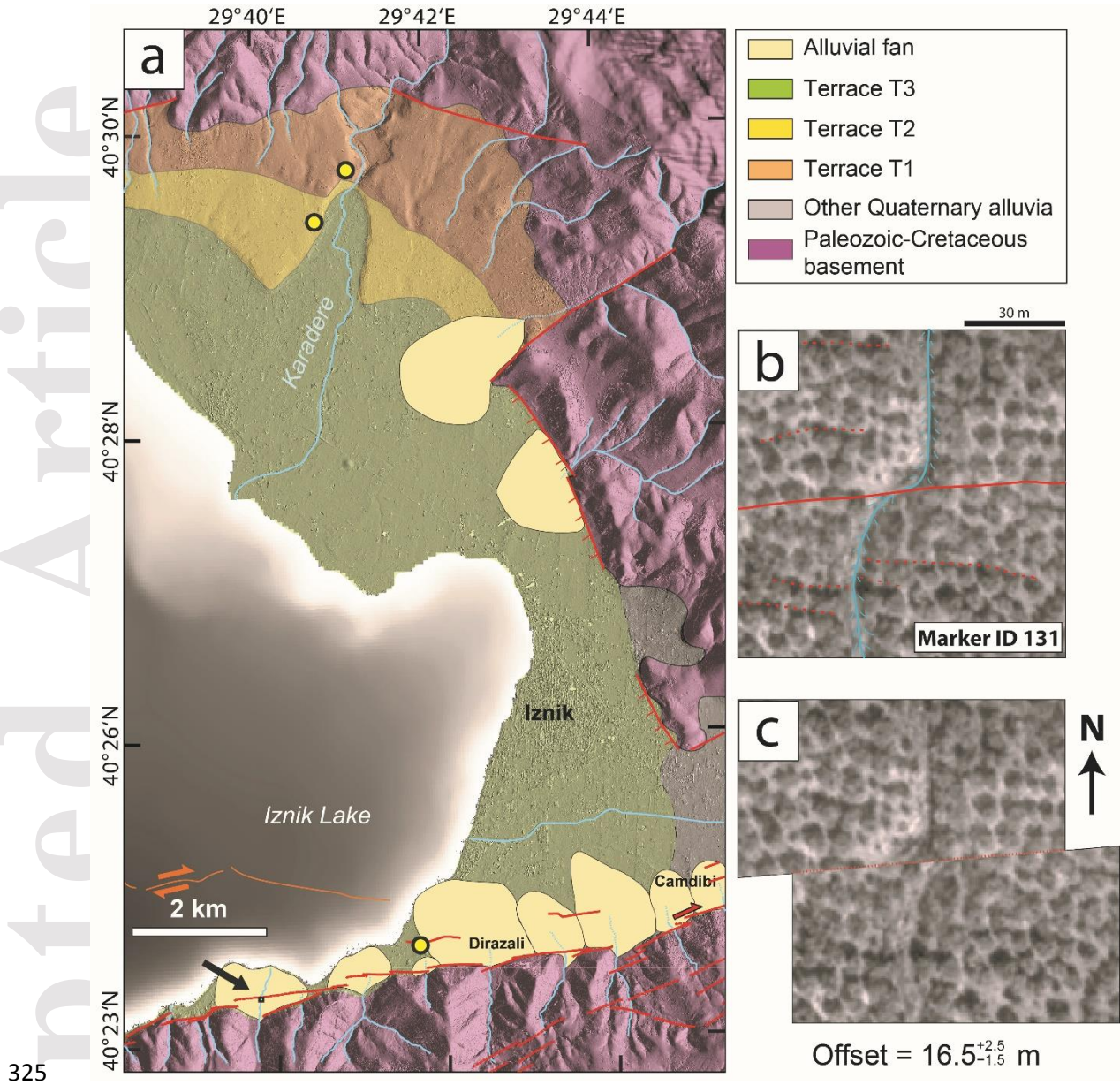
Figure 9. (a) General location of the terrace sampled for cosmogenic dating (yellow dots). Active faults are mapped in red-orange and main streams are drawn in blue. The subaqueous fault trace is taken from Gastineau et al. (2021). The eastern limit of terrace T3 is not well defined in the geomorphology and was drawn assuming a constant elevation. The marker used to derive a minimum horizontal slip rate is indicated with a black arrow. (b) Interpreted Pleiades image of the present-day marker morphology. (c) Preferred retro-deformed morphology.

Schematic log   Lithological description

a — T3

m
0
— hard, dark brown soil with few, centimetric pebbles
— light brown, sandy layer, numerous pebbles
1
— brownish grey clay layer
2
— coarse silt layer, heterogeneous unsorted pebbles

b — T2

m
0
— thin brown soil with few gravel
— dark brown silty layer with few pebbles
0.5
— brown sandy layer, homogeneous rounded pebbles
— light brown, gravel-rich sandy layer with few pebbles
1
1.5
— coarse, orange sandy layer, abundant pebbles and gravel

c — T1

m
2.5
— sandy layer, gravel and heterogeneous pebbles
— fine sandy layer with gravel and few pebble
3
— coarse sandy layer with large, subrounded pebbles
— sandy layer with abundant small pebbles
3.5
— fine, gravel-rich sandy layer
— sandy layer, homogeneous rounded pebbles
4
— very fine silty-sandy layer

332

Figure 10. Field photographs (left) and interpreted stratigraphy (right) of the terrace profiles

sampled for dating, T3 (a), T2 (b), and T1 (c). The samples are represented with white circles.

The first meters of T1 profile were covered with bushes, and consisted of a homogeneous brown,

silty-sandy unit with a few centimetric pebbles.

337   Actually, the statistical analysis of cumulative offsets evidences the occurrence of past ruptures

338   along the MNAF and documents the associated slip-per-event, but does not inform the age of

339   these events. To narrow down the age range for the identified events and estimate the late

340   Quaternary slip rate of the MNAF, we need constraints on the age of the terranes that were offset

341   by the fault. The area surrounding Iznik Lake displays low gradient alluvial fans emplaced on

342   three preceding levels of abandoned lake plains, which were targeted in this study. These flat

343   levels, separated by wave-cut scarps, have been known and interpreted as lacustrine terraces

344   since the early 20th century (Chaput, 1936; Tanoglu and Erinc, 1956). They appear particularly

345   well-developed north and east of Iznik Lake (Ikeda et al., 1991; Fig. 9a). The terraces were

346   presumably deposited originally with a small slope, but the current slope tends to increase with

347   elevation and age, and also in the central part as the terraces get closer to the mountain range.

348   The lowest scarp associated with the youngest lake plain (Tl3) is the clearest and can be traced

349   almost over the entire length of the northern coast. The height of its inner edge above the present

350   lake level (a.l.l.) is about 20 meters northwest Boyalica village. The intermediate terraceT2 can

351   also be easily traced in the west but is hardly visible in the central part around Boyalica. The

352   associated wave-cut scarp appears again in the wider alluvial plain northeast of the lake, with an

353   inner edge 60 m high a.l.l. The highest and oldest terraceT1 is much more degraded but can still

354   be traced almost continuously in the west with a 110 m a.l.l. high inner edge. Remnants of this

355   old paleoshoreline and the associated sediments can be observed in the northeast, especially

356   along an irrigation canal constructed west of the Karadere stream. In the southern part, these

357   successive terrace levels cannot be unambiguously mapped and have been partly overlain by

358   younger alluvial sediments, especially in areas where the lake shore comes very near to the foot

359   of the mountain front.

6.1 Sampling and analytical method

To date the terraces, we used the *in-situ* produced terrestrial cosmogenic nuclide (TCN) method. The terraces were sampled along vertical profiles (Fig. 10, Table 5). For terraces T1 and T2, samples were taken on pre-existing, man-made scarps. These scarps have been laterally refreshed due the surrounding agricultural activity, preventing a significant nuclide accumulation from posterior lateral exposure. For terrace T3, we benefited from a pit dug in the plain for hydrological maintenance. The pit is located close to the western edge of the major fan of Dirazali, so an alluvial contribution posterior to the emersion of the lake plain cannot be ruled out. The outcrops displayed alternations of fine sand and coarser gravel-rich conglomerate with graded bedding, with no evidence of buried paleosols. T1 and T3 mainly showed alluvial facies, the former displaying evidence of paleochannels and cross-stratification. T2 showed lateral facies variations, with finer, lacustrine deposits on the north-central shore of the lake, and coarser fluvial deposits in the east at the sampling site. While T1 and T3 profiles can be assumed to represent a continuous sedimentation sequence, T2 profile displays an irregular interface at 1 m depth that suggests an interruption in the sedimentation process potentially associated with emersion and erosion (red line on Fig. 10b). For each profile, we collected two samples on the surface of the terrace, and when possible, three to four samples in the first 1.5 m below the surface, and one to two deeper samples at the bottom of the profile to constrain the potential inherited nuclide content. We sampled pebbles made of silicate material in order to have ~100 g of quartz per sample.

The beryllium was extracted at the Geo-thermo-chronology platform (ISTerre, University Grenoble Alpes, France). Quartz was obtained from the 250-500 µm fraction after isolation of the non-magnetic grains by repeated leaching in a H_2SiF_6-HCl mixture. The samples were then

383 processed following the chemical procedure of Brown et al. (1991) and Merchel and Herpers

384 (1999). The beryllium was finally measured as a $^{10}Be/^{9}Be$ ratio at the ASTER Accelerator Mass

385 Spectrometer in Aix-en-Provence, France (Arnold et al., 2010).

6.2 Age determination

387 The obtained concentration-depth-profiles (Table 5 and Fig. 11, 12, 13) were modelled with a

388 Monte Carlo approach using the code ^{10}Be profile simulator version 1.2 developed by Hidy et al.

389 (2010). This approach enables to find the combination of parameters that best fits the measured

390 profile, including the exposure age, the erosion rate and the inherited TCN concentration. The

391 validity of the method requires the following conditions: the TCN concentrations have not

392 reached equilibrium with the landscape, the sampled profile corresponds to a unique episode of

393 deposition and exposure with no vertical mixing, the inherited concentration is constant over the

394 sampled depth range.

395 The halflife of ^{10}Be (1.387±0.012 Ma) was taken from Chmeleff et al. (2010). We used a global

396 mean SLHL (sea level and high latitude) reference production rate of 4.06±0.23 atoms.g^{-1}.a^{-1} for

397 the neutron induced spallogenic production using the CREp program (Martin et al., 2017), with

398 the Lifton-Sato-Dunai scaling scheme (Lifton et al., 2014), the ERA40 atmosphere model

399 (Uppala et al., 2005), and the Lifton VDM 2016 geomagnetic correction (Lifton, 2016). The

400 muonic production was calculated using the theoretical equations of Heisinger et al. (2002a,b)

401 and determined at the sampling site's elevation and for a given depth following the approach of

402 Balco et al. (2008). The depth of muonic production fit was set at 5 cm. The error in 10Be half-

403 life was set at 5%. The sampling sites were not associated with significant topographic/geometric

404 shielding or additional cover. The cumulative bulk density of the material above each sample

405   was assumed constant over depth, with an average value of 2.2 g/cm^3, previously measured in

406   similar gravel-based terraces (Hidy et al., 2010). For the first iterations, the initial parameters for

407   age, inheritance and erosion rate were allowed to vary largely (age between 5-40 ka, erosion rate

408   below 3 cm/ka, and inheritance below 25.105 at/g). The total erosion threshold was set between
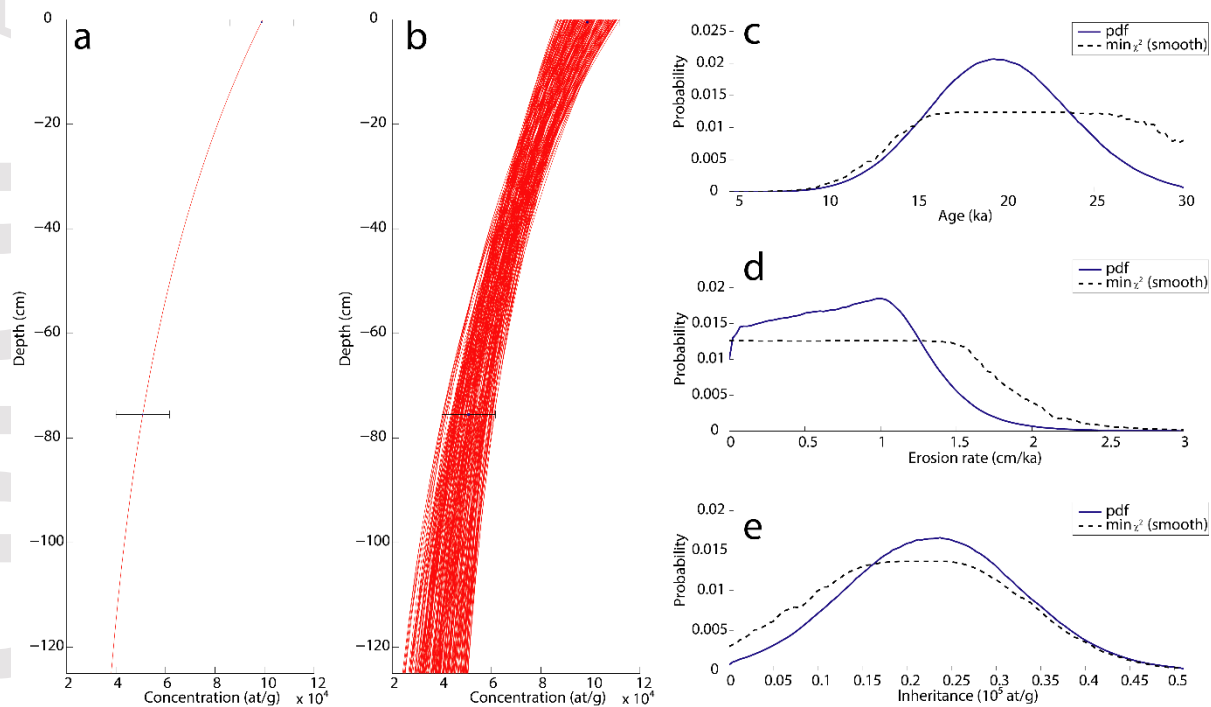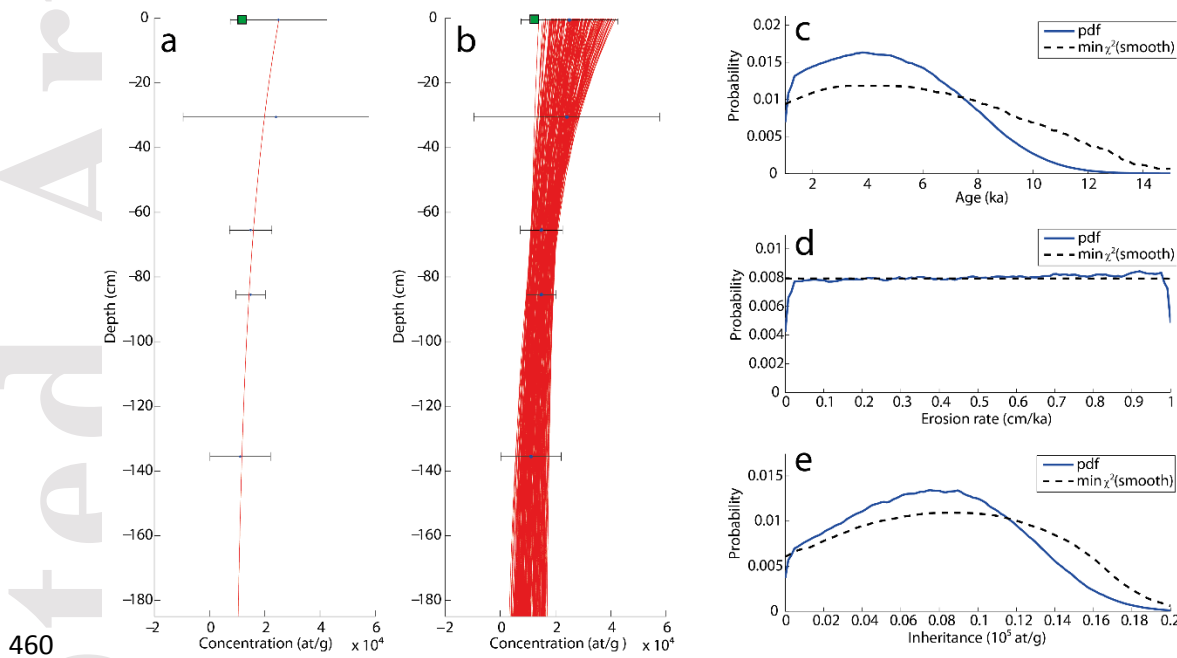
409   0 and 30 cm.

410
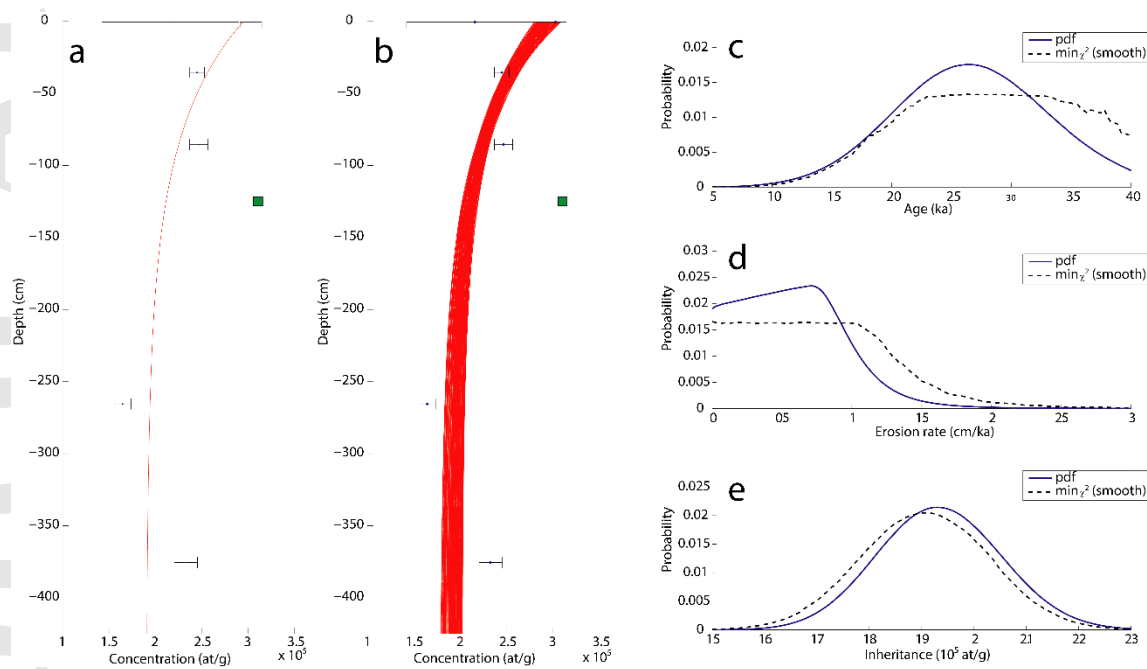
411

412   **Figure 11.** Result of the Monte Carlo simulations for terrace T1. (a) ^{10}Be concentrations

413   measured along depth and best fit obtained. (b) All the solutions found in the parameter solution

414   space defined as inputs. The sample excluded from the inversion is shown as a green box. (c, d,

415   e) Probability density functions (solid lines) and minimum χ^2 distributions (dashed line) for the

416   exposure age, erosion rate and inheritance concentration respectively.

417

418   Terrace T1 profile presents one point (15TUR4-130) with a high concentration, larger than the

419   surface samples, which is incompatible with the theoretical depth profile. After excluding this

420   sample, the algorithm was not able to find solutions in the 2σ confidence windows, and we had

421   to increase the χ^2 cut-off value to 11. Although doing so prevented us from properly quantifying

422   the error on the parameters, the best fits among the 250,000 solutions obtained provided a modal

423   age of $\mathbf{27.0^{+10.9}_{-13.0}}$ ^{10}Be ka BP (Fig. 11), a low erosion rate ranging below 1 cm/ka, and a much

424   higher inheritance around ~190,000 at/g.

425

426

427   **Figure 12.** Result of the Monte Carlo simulations for terrace T2. (a) ^{10}Be concentrations

428   measured along depth and best fit obtained. (b) All the solutions found in the parameter solution

429   space defined as inputs. The three samples excluded from the inversion show concentrations

430   above 120,000 at/g. (c, d, e) Probability density functions (solid lines) and minimum χ^2

431   distributions (dashed line) for the exposure age, erosion rate and inheritance concentration

432   respectively.

433   Terrace T2 profile presents more complexity, especially because the two deepest samples

434   (15TUR3-110 and 15TUR3-150) have the highest nuclide concentrations of all the dataset. As

435   the outcrop stratigraphy suggests, they are likely to belong to a previous deposition sequence

436   which was eroded before the onset of a new sedimentation sequence over it. The algorithm could

437   only converge towards a solution after excluding these deep samples, and one surface sample

438   (15TUR3-0a) showing a low nuclide concentration. With only two samples, it is impossible to

439   determine statistically robust solutions for the age, erosion rate and inheritance at the same time.

440   To narrow down the solution space, we constrained the initial inheritance using the concentration

441   of sample 15TUR3-60 as upper bound, and the initial age below the age obtained for T1. We

442   finally obtained 250,000 solutions within the 2σ confidence window, giving a most probable age

443   of $\mathbf{19.6^{+7.7}_{-7.2}}$ [10]Be ka BP (Fig. 12).

444   For terrace T3, the simulator was not able to produce solutions when all the data of the profile

445   were included, especially because one surface sample (15TUR5-0a) showed a very low

446   concentration comparable to the deepest sample (15TUR5-130). We assumed this sample to be

447   an outlier, likely to originate from recent excavation and deposition during agricultural work. We

448   observed that the profile data did not permit to constrain the erosion rate. We tested initial

449   maximum erosion rates of 1, 2 and 3 cm/kyr and obtained similar results between the three

450   simulations. Using a moderate erosion rate of 1 cm/kyr as initial upper bound, the 250,000

451   solutions found within the 2σ confidence window gave a most probable age of $\mathbf{3.8^{+6.3}_{-2.7}}$ [10]Be ka

452   BP. This involves an inheritance of ~8000 at/g (i.e. 30% of the surface sample) (Fig. 13e).

453   Finally, we considered the possibility that additional exposure may happen under a shallow lake

454   water cover, which would lead to an overestimation of the age of subaerial exposure, as TCN

455   started to accumulate before the total emersion and abandonment of the lake plain. A water depth

456   of 4 m allows ~10% of the influx of cosmic rays to hit the sediments. To estimate the amplitude

457   of this effect on the final age, we ran the simulation with the nuclide concentrations decreased by

458   10%. This correction resulted in a 16% younger age, which suggests that this effect remains

459   small relative to the 2σ uncertainty range.

460

461   **Figure 13.** Result of the Monte Carlo simulations for terrace T3. (a) [10]Be concentrations

462   measured along depth and best fit obtained. (b) All the solutions found in the parameter solution

463   space defined as inputs. The sample excluded from the inversion is shown as a green box. (c, d,

464   e) Probability density functions (solid lines) and minimum χ^2 distributions (dashed line) for the

465   exposure age, erosion rate and inheritance concentration respectively.

466

467 **7 Discussion**

468 **7.1 Horizontal slip rate estimate**

469 Horizontal slip rates are usually constrained by dating sedimentary units laterally displaced by

470 the faults (Hubert-Ferrari et al., 2002; Kozaci et al., 2007, 2009; Le Béon et al., 2010; Rizza et

471 al., 2011; van der Woerd et al., 2006; Zabci et al., 2015). This kind of estimation is preferentially

472 done with cumulative offsets of several hundreds of meters in order to average out the variability

473 of individual coseismic displacements (see e.g. Wechsler et al., 2018). This type of measurement

474 will yield a minimum slip rate as the offset is considered to be as old as the emplacement of the

475 sediments, although it could also be much younger without a way for us to know about it.

476 Southeast of the lake, the MNAF segments have displaced Holocene streams incising in the low-

477 gradient alluvial fans overlying terrace T3. Among the markers identified, the largest quality 1

478 offset measured is $\mathbf{16.5^{+2.5}_{-1.5}}$ m on a river located ~3.5 km west of Dirazali village (Fig. 9). The

479 COPD results suggest that this corresponds to the cumulative slip of the last 3 to 4 large

480 earthquakes. Deriving a slip-rate from this offset and our age of $\mathbf{3.8^{+6.3}_{-2.7}}$ [10]Be ka BP for T3 is

481 hampered by two limitations. (i) The displaced stream may be significantly younger than the

482 underlying lake plain, so the ratio between the mean offset and the age of T3 can only provide a

483 minimum horizontal slip rate. (ii) The possible alluvial contribution at the sampling pit from the

484 Dirazali fan must be assumed synchronous or older than the fan incised in by the offset stream.

485 To propagate the 2σ asymmetric uncertainties in the slip rate calculation, we used the NIST

486 Uncertainty Machine (https://uncertainty.nist.gov/; Lafarge and Possolo, 2016) with a Monte

487 Carlo approach. We obtained a horizontal slip rate of $\mathbf{4.4^{+10.6}_{-2.8}}$ mm/yr. Although this value is in

488 the same range as the rate of 3.7±0.7 mm/yr estimated by Gasperini et al. (2011) on Gemlik

489   segment, it is poorly constrained due to the young age and large relative uncertainty of T3.

490

7.2 Past seismic events evidenced along-strike

492   Our study of cumulative offsets along the MNAF provides valuable information on earthquake

493   propagation along this fault, in terms of rupture extent, slip amount and distribution. It also

494   allows us to discuss the behavior of the MNAF segments during the last major earthquakes.

495   If we assume the first two peaks to be the signature of the last two large earthquakes, with

496   respective maximum coseismic slips of 6.2 ± 2 m and 5.7 ± 4 m, empirical scaling laws suggest

497   that they correspond to events of moment magnitude of 7.2 ± 0.2 to 7.4 ± 0.2, with rupture lengths

498   of 73 ± 28 to 97 ± 42 km (Wells & Coppersmith, 1994; using all-slip-type and strike-slip

499   regressions respectively). Conversely, a rupture extending along the entirety of the 148 km long

500   studies section would correspond to an earthquake of moment magnitude 7.6 ± 0.3 and maximum

501   coseismic displacements of 6.7-6.8 m, using the same scaling relationships. Our results are

502   therefore compatible with large earthquakes able to rupture large parts of the eastern MNAF.

503   Wesnousky (2006) has suggested that there exists a maximal step-over size (3-4 km fault-

504   perpendicular) which tends to stop rupture propagation. However, this threshold has been

505   crossed in recent examples (e.g. Fletcher et al., 2014; Hamling et al., 2017). In our case, Sölöz

506   bend and Mekece, which are the largest identified step-overs of the eastern MNAF, have widths

507   of 2.5 and 1.5 km respectively, and it can thus be assumed that past large ruptures may have

508   propagated through them.

509   Our results show significant along-strike variability of the total number of recorded slip events

510 and the associated slip values. Mean slip values tend to be lower for segments C, D and E. We

511 also note that segments D and E document more individual slip events than the other segments. It

512 has been observed that the COPD curve shows an exponential decay in the peaks' amplitude

513 with increasing cumulative slip (Klinger et al., 2011), as older markers tend to be less preserved

514 in the landscape. We find this kind of pattern for some segments (e.g. segment C), but for

515 segments B and G we observe that peak 1 is smaller than peak 2. The central segments are

516 characterized by higher slopes. This implies more dynamic hydrologic conditions and

517 geomorphic marker formation, and thus a higher capacity to preserve the traces of successive

518 earthquakes (Zielke et al., 2015). By contrast, the lower slopes of the other segments may have

519 favored more intensive agricultural activities, thus partly erasing traces of past ruptures.

520 Therefore, a first possibility to explain the along-strike slip-per-event variability is to assume that

521 COPD peak 1 on segments B, F and G is cumulative, and that the last event was not preserved

522 enough on segments B, F and G to produce a strong COPD peak (Fig. 14b).

523 Alternatively, the slip decrease observed in the central segments may be related to their higher

524 geometrical complexity (fault bends and obliquity, overlapping segments and branching, see

525 sections 2 and 4.2). Distribution of the deformation across several structures implies that only

526 part of the slip can be measured on the investigated MNAF strand, leading to apparent local slip

527 decrease. A more oblique slip vector with a larger, unaccounted for vertical component,

528 especially along segments C and D, may have a similar effect. Lower horizontal coseismic slip

529 values along these segments may also suggest partial partitioning, with the subaqueous Iznik

530 fault accommodating a part of the horizontal displacement (see e.g. de Michele et al., 2010; King

531 et al., 2005 for recent examples of this). Finally, structural complexities may act as a barrier for

532 the propagation of ruptures, leading to smaller offsets through slip tapering (King and Nabelek,

533   1985; Ward, 1997; Zielke et al., 2015).
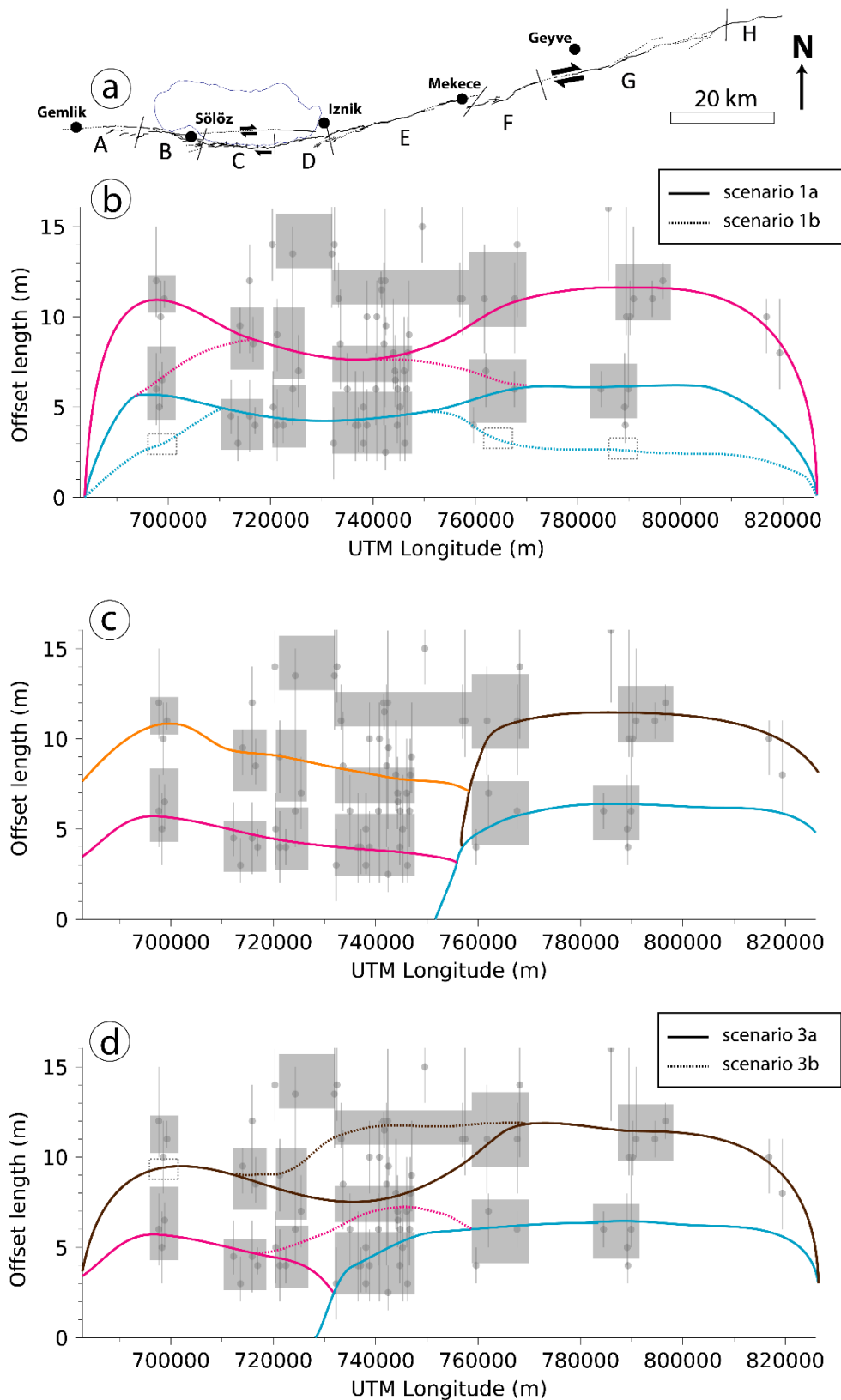
535 **Figure 14.** (a) Geometry of the fault section studied. (b) First order scenarios of horizontal slip

536 distribution during past events. The last major event (light blue) is assumed to have ruptured all

537 the segments. The penultimate (magenta) replicates this slip distribution. Alternative scenario 1b

538 assumes a partly unpreserved, smaller slip (broken boxes) for the last major rupture. (c) Scenario

539 2 of horizontal slip distribution. The last rupture is assumed to have propagated in the east of the

540 section studied and along segments F to H. The penultimate event propagated along the

541 remaining segments and further west. The previous events (brown and orange) replicate these

542 slip distributions. (d) Scenario 3 of horizontal slip distribution. The last ruptures propagated

543 partially along the MNAF and neighboring systems. The antepenultimate event (brown) was a

544 full MNAF rupture with a partly unpreserved smaller slip on segment A. Alternative scenario 3b

545 assumes overlapping traces for the last ruptures on segment D.

546

547 The combination of the coseismic slip variation along strike, the epistemic uncertainty affecting

548 offset measurements and the evolution of markers' morphology since the last event can limit the

549 interpretation of COPD peaks as representing individual earthquakes (Lin et al., 2020; Reitman

550 et al., 2019). Given that the last large earthquake along the MNAF happened before the 20th

551 century and was not accurately documented at the time, we ignore the typical range of variation

552 for the coseismic slip. The surface slip during 1999 Düzce and Izmit earthquakes on the NNAF

553 show coefficients of variation (CoV) of 0.5-0.6 (Akyüz et al., 2002; Barka et al., 2002). Such

554 values of CoV hardly enable to confidently recover more than one or two events or sequence of

555 events from the COPD curve and estimate the associated slip values. Therefore, higher COPD

556 peak values and increments, which come with higher uncertainty, should be considered with

557 caution. A couple of slip increments on segments B and E exceed 6.5 m (Table 4) and seem less

558   realistic given the magnitudes typically observed for recent earthquakes and estimated for

559   historical earthquakes in the Marmara region. Thus, we interpret those as being cumulative

560   contributions of two or more smaller, distinct events.

561   The slip history per segment resulting from our offset analysis does not unambiguously unravel

562   the past earthquakes succession along the MNAF. Alternative scenarios, with different numbers

563   of earthquakes, locations, lengths of ruptures, can be proposed that account equally for these

564   observations. Given the resolution of our satellite images and the uncertainties in our offset

565   measurements, our analysis can hardly detect individual offsets below 2.5 m and thus slip events

566   of Mw < 7. We cannot rule out that some smaller slip events were not resolved by our analysis,

567   which would add some local variability of the slip distribution in the possible scenarios. The

568   amount of slip involved in these events would logically be smaller as well, and so the

569   uncertainties associated with them would not fundamentally change the proposed scenarios.

570   To assess the possible scenarios, we require independent constraints about the location, age and

571   characteristics of past earthquakes along the MNAF. Fortunately, the seismicity of the MNAF

572   region of the last two millennia is documented by significant written accounts (see e.g.

573   Ambraseys, 2009), archeological evidence (Benjelloun et al., 2018, 2020) and a few

574   paleoseismological investigations (see section 3). According to the slip rate estimates (sections 3

575   and 7.1), this time frame should correspond to a cumulative horizontal slip ranging between 6

576   and 10 meters. This includes between one and three COPD peaks, depending on segments.

577

578

579 **7.3 Independent constraints on historical earthquakes along the MNAF**

580 **7.3.1 Historical seismicity**

581 At least five destructive ruptures are documented in the historical seismicity catalogues for the

582 eastern part of the MNAF (Ambraseys, 2002, 2009; Ambraseys and Finkel, 1991, 1995;

583 Ambraseys and Jackson, 1998; Guidoboni et al., 1994; Fig. 2; Table S1). These events come

584 with high uncertainties on their location and magnitude, and it is generally difficult to locate the

585 ruptured fault from historical data only. Most of the information available relates to the cities of

586 Iznik and Gemlik. Excluding the earthquakes documented on the NNAF, Iznik was destroyed by

587 local earthquakes around 29-32 CE (M_s 7), in 121 CE (M_s 7.4), in 368 CE (M_s 6.8), and 1065 CE

588 (M_s 6.8). The region of Gemlik was affected by the M_s~7.2 1419 CE earthquake, which may

589 have originated from the SNAF system as no effect was reported in Iznik. A series of minor

590 ruptures, with estimated magnitudes about 5, are known between 1855 and 1863, also felt in

591 Gemlik and along the southern shore of Iznik Lake.

592 **7.3.2 Archeoseismology**

593 Through an archeoseismological study in Iznik, Benjelloun et al. (2020) evidenced three

594 episodes of seismic damage in the city since the Roman period: (1) between the early 6th and late

595 8th century CE, (2) between the mid-9th and late 11th century CE, and (3) after the late 14th

596 century CE. These episodes were associated with a minimal intensity of VIII (EMS-98) in Iznik,

597 suggesting earthquakes of at least Mw 6. The modeling of a standing Roman obelisk north of the

598 city ruled out the occurrence of Mw > 7.2 ruptures along the fault section south of Iznik since the

599 1st century AD.

7.3.3 Paleoseismology

600

601 Paleoseismological trenching works have documented mid-19th century events on segments A

602 and C. On segment A, a penultimate event was identified between the 12th and 18th centuries CE,

603 but was not seen in trenches located south of Iznik Lake. A possibly contemporaneous event was

604 also documented between the 14th and 18th centuries in a trench west of Mekece. On segment C,

605 one penultimate event was documented after the late 7th century CE, and two older events were

606 identified before the mid-5th century CE in two trenches (see section 3, Fig. 2c). South of Iznik

607 Lake, Erginal et al. (2021) reported a 50 cm high coseismic scarplet in beachrock deposits that

608 they attributed to an 8th century rupture.

609 Other important constraints can be derived from the lake core recently studied by Gastineau et al.

610 (2021). These sedimentary archives recorded the occurrence of several major earthquakes

611 documented both on the NNAF and MNAF, among which the 29-32 CE, 121 CE, 1065 CE, and

612 an 8th century CE event. The 1065 CE earthquake ruptured a sublacustrine fault trace identified

613 within Iznik Lake, north of the onshore segment D. No event was recorded in these cores in the

614 eight centuries following the 1065 CE earthquake, which strongly supports the absence of Mw >

615 6.5 events on the central segments of the MNAF after 1065 CE. However, the lack of earthquake

616 recording after 1065 may be due to too low sedimentation rates in the lake in the last millennium,

617 even for large events located farther than 20-30 km from the lake.

7.3.4 Synthesis

618

619 The events documented by at least two types of record, include the 29-32 (M_s 7), 121 (M_s 7.4),

620 1065 (M_s 6.8) and 1419 (M_s 7.2) CE historical earthquakes. The precise location of the 1419 CE

621 earthquake is not well constrained, but the fact that it was not recorded in the Iznik Lake cores

622   nor in trenches south of Iznik Lake, and that destructions were only reported in the region of

623   Bursa, suggest that it did not extend east of Sölöz. To these we can add an 8th century event

624   which affected the central MNAF segments south of Iznik Lake, and a 14th-18th century event

625   attested by some damaged buildings in Iznik and one trench on segment E.

626

627   **7.4 Analysis of COPD peak 1**

628   In a first assumption (Fig. 14b, scenario 1a), COPD peak 1 can be interpreted as a large Mw 7.2-

629   7.4 event rupturing the whole length of the studied fault. This first interpretation involves

630   significant slip variations along strike, with slip values on the central segments C, D and E ~33%

631   lower than on the other segments. The hypothesis of differential preservation across segments

632   suggests another scenario (Fig. 14b, scenario 1b), with a more homogeneous slip of ~4 m along

633   the studied section, only recovered on the central segments. Instead of decreasing slip on the

634   central segments as in the scenario 1a, this scenario involves a maximum slip in the central area,

635   which decrease towards both rupture tips. Given the higher structural complexity of this area,

636   lower horizontal slip values are expected along the central segments. Therefore, scenario 1a can

637   be considered more likely than scenario 1b. The favored historical candidate is the 1065 CE

638   earthquake, which is the best documented event. However, this means that the magnitude of the

639   1065 CE earthquake, estimated at 6.8 by historical seismology studies, should be significantly

640   raised, by at least 0.3 units. It also implies that the 1065 CE rupture identified in Iznik lake

641   propagated along the onshore fault segments as well. In addition, the deformation of the obelisk

642   north of Iznik does not support magnitudes over Mw 7.2 for events located south of Iznik, but

643   might be accounted for with a more distant epicenter, located on the western or eastern segments

644   (Benjelloun et al., 2020).

645   Another possibility is to propose earthquakes rupturing only a part of the studied MNAF section,

646   with the central segments acting as a slip barrier (Fig. 14c, d). Following this hypothesis, COPD

647   peak 1 would correspond to two different earthquakes. These earthquakes ruptured different

648   sections of the fault, either adjacent (scenarios 2 and 3a) or overlapping (scenario 3b). The lower

649   slip values on the central segments are associated with the termination of earthquakes. In this

650   case, no significant slip variation appears along strike. The high slip values imply that the

651   ruptured area during these earthquakes could be respectively extended west of Gemlik and east

652   of the junction with the main NAF strand. This interpretation best accounts for the multiple

653   events found in the different records of past seismicity. The 1065 CE earthquake is a favored

654   candidate for the western and central segments. The historical seismicity of the east of the

655   studied area is less documented, but the 14th-18th c. event found in the archeological and

656   paleoseismic record is a possible candidate for the eastern rupture of this scenario.

657

658   **7.5 Analysis of COPD peak 2 and implications for the long-term behavior of the MNAF**

659   The increments between COPD peaks 1 and 2 suggest that the slip values of the last and

660   penultimate events (or sequences of events) were comparable. Although the slip values estimated

661   for the penultimate event come with higher uncertainties, they also suggest magnitudes as high

662   as Mw 7.4±0.2. The lacustrine record documents at least two events in the first centuries CE

663   (Gastineau et al., 2021). The historical catalogues include two candidates, in 29-32 CE and in

664   121 CE, with poorly constrained locations along the MNAF. Both events can be accounted for

665   by interpreting peak 2 as two distinct ruptures (scenario 2, Fig. 14c). Given the uncertainties, a

666   full MNAF rupture may also be proposed (scenarios 1 and 3, Fig. 14b and d).

667   The reconstructions of along-fault slip accumulation derived from systematic offset

668   measurements have been associated to the development of earthquake recurrence models

669   (Schwartz & Coppersmith, 1984; Zielke et al., 2015). In our case, given the large uncertainties,

670   the successive increments on each segment cannot be unambiguously discriminated. Our dataset

671   remains compatible with a "characteristic slip" behavior, as in scenarios 1 and 2 (Fig. 14b, c),

672   where the earthquakes show recurring, similar slip distributions (see e. g. Klinger et al., 2011;

673   Kurtz et al., 2018; Zielke et al., 2010). In scenarios 1a and 2, the horizontal cumulative slip on

674   segments C, D and E is 25-35% lower than on the other segments for the last two events. This

675   cumulative slip deficit on the central segments produces a higher apparent slip rate variation

676   along-strike. The interpretations of scenario 3 depart from the characteristic slip model, as the

677   proposed distributions of the last events differ from the previous one, which resembles a variable

678   slip model.

679   The Late Quaternary slip accumulation along the MNAF seems dominated by large events with

680   comparable per-segment slip increments. This corresponds to the synoptic model of Zielke et al.

681   (2015), which also considers the occurrence of smaller ruptures contributing marginally to the

682   overall slip accumulation. The 8th century CE event reported south of Iznik Lake (Erginal et al.,

683   2021), and the 19th century CE earthquakes reported in Gemlik (Özalp et al., 2013) may illustrate

684   these features. Future trenching work is needed to document the timing of earthquakes and to

685   judge between both models.

686

687

7.6 Possible interactions between the NAF strands for the historical period

In all the scenarios discussed, we can propose that the eastern MNAF has experienced two major

sequences of ruptures in the last two millennia. These historical sequences correspond to large

magnitude events, with amounts of slip ranging between 3.2 and 6.2 m. Most of the deformation

was produced during intervals of high seismic activity, separated by longer quiescent periods

(1000-1500 years). This can be compared to the rupture history of other strike-slip fault systems

such as the San Andreas and Dead Sea faults (Lefevre et al., 2018; Rockwell et al., 2014). This

long recurrence time contrasts with the historical behavior of the NNAF (Fig. 2), and is

consistent with a slip rate ~5 times smaller on the MNAF. In the final part of this discussion, we

replace our propositions of past rupture history in the wider frame of the eastern Marmara region.

The last sequence of high seismicity along the MNAF, whatever the scenario considered, seems

to occur between the 11th and 18th centuries, while the northern strand of the NAF along the

Izmit Gulf (between 29.2° and 30.3°E) knew a period of lower seismic activity (Fig. 2b). The

1065 CE earthquake was preceded by a major event on the NNAF in 1063 CE. However, it

mainly affected the western part of the Marmara region, with no significant damage reported east

of Constantinople (Ambraseys, 2009). Between the 14th and 18th centuries, only one major

earthquake is known for the eastern Marmara region in 1509 CE (M~7.2). The Gulf of Izmit was

likely affected by this earthquake (Klinger et al., 2003), but the contemporary historical records

do not account for heavy damage farther east (Ambraseys, 2001b). After this earthquake, a

quiescence period is reported for the Marmara region between 1509 and 1719 CE (Ambraseys &

Jacskon, 2000; Pondard et al., 2007; Rockwell et al., 2009).

By contrast, the southern strands of the NAF were marked by a significant seismic activity in the

710   east of the Marmara Sea. After the 1065 CE earthquake on the MNAF, this activity seems to

711   restart in the early 15th century CE. It includes the 1419 CE earthquake which affected the Bursa

712   region, and the event proposed between the 14th and 18th centuries CE along the eastern segments

713   of the MNAF (scenarios 2 and 3). This earthquake may have propagated across the junction with

714   the main NAF strand. The junction zone does not present any significant step-over, but only an

715   azimuth change of ~20°. The 1967 CE earthquake propagated across this junction between the

716   main NAF and the NNAF, with a similar azimuth difference. Therefore, a symmetrical rupture

717   between the main NAF and the MNAF is not unrealistic. A trenching study carried out by

718   Palyvos et al. (2007) in the Mudurnu valley, located a few kilometers east of the junction with

719   the main NAF strand, identified at least one and most probably two paleoevents younger than

720   1693 CE. Some of these ruptures may have propagated across the junction along the MNAF.

721   Analogous alternations of active and quiescent phases between adjacent fault strands have been

722   previously identified on the San Andreas fault system in relation to the San Jacinto fault (Lozos,

723   2016; Onderdonk et al., 2018). In the case of the NAF in the Marmara region, the investigation

724   of older sedimentary records of past earthquakes on the different strands might better document

725   this behavior and check for earlier occurrences of it.

726

727   8 Conclusion

728   By combining field observations and the analysis of high-resolution satellite images, we have

729   demonstrated that the segments constituting the MNAF in the southeast of the Marmara region

730   have been significantly active during the Holocene. The fault displays morphological features

731   typical of strike-slip deformation, associated locally with a smaller vertical component. We

732   collected 114 measurements of horizontally offset markers, providing evidence for large,

733   repeated earthquakes along the MNAF. Through a statistical analysis of the offsets, we

734   particularly documented at least two major surface-rupturing earthquakes whose deformation

735   was preserved in the landscape. They are characterized by coseismic horizontal displacement

736   ranging from 3.2 to 6.2 m, which indicates moment magnitudes ranging between 7.2±0.2 and

737   7.4±0.2 according to empirical scaling laws. Some of these events may have ruptured the whole

738   eastern MNAF section along more than 100 km. Although smaller earthquakes also happened in

739   the past, our analysis may not resolve accurately their frequency due to the data uncertainties and

740   preservation issues. According to the historical catalogues of seismicity and paleoseismological

741   studies, the last large events documented along this fault strand possibly happened in 1065 CE,

742   or between the 14th and 18th centuries CE along the eastern segments. These intervals correspond

743   to a period of relative quiescence along the NNAF segments located east of the Marmara Sea.

744   We estimated a late Holocene horizontal slip rate of $4.4^{+10.6}_{-2.8}$ mm/yr on the central MNAF

745   segments. Since the last large events, the eastern MNAF segments may have accumulated stress

746   equivalent to 1-4 m of horizontal deformation. Therefore, the current level of stress may be

747   enough to generate a significant earthquake, comparable or larger than a 1065 CE type rupture,

748   which caused important damage in Iznik. The activity of the southern strands of the NAF should

749   not be neglected in terms of slip history and should be considered into any seismic hazard

750   assessment.

751

752   **Data Availability Statement**

753   The bathymetric map of Marmara was made available by the EMODnet Bathymetry project

754   (https://www.emodnet.eu/bathymetry), using the EMODnet Bathymetry portal (EMODnet

755   Bathymetry Consortium, 2016, EMODnet Digital Bathymetry [DTM], DOI:

756   10.12770/c7b53704-999d-4721-b1a3-04ec60c87238) funded by the European Commission

757   Directorate General for Maritime Affairs and Fisheries. The large-scale topography of the study

758   area was obtained from the Shuttle Radar Topography Mission 1 Arc-Second Global

759   (DOI:10.5066/F7PR7TFT). The bathymetry of İznik Lake was provided by and can be obtained

760   from the Turkish General Directorate of Hydraulic Works (DSI). Pleiades imagery is available

761   for purchase from Airbus industry (https://www.intelligence-airbusds.com/en/8692- pleiades).

762   The full offset retro-deformation dataset and a vector file of the fault map are available on the

763   Zenodo repository (Benjelloun et al., 2021) [open access]. The maps of Figures 5 are from

764   Google Earth satellite imagery. The diagrams of Figures 6, 7, 8 and 14 were prepared using the

765   Matplotlib 3.3.0 package for Python (https://matplotlib.org/; Hunter, 2007). All websites were

766   last accessed in January 2021. Supporting Information for this article includes a detailed

767   explanation of the marker quality score determination, a list of historical earthquakes in the area

768   of interest, a summary of paleoseismic trenching works done in the area, the offset measurement

769   data, and supplementary figures on the vertical slip markers south of Iznik Lake, some field

770   examples of Quaternary faulting, and the automatic fault discretization procedure.

771

785

References

787   Aki, K. (1984). Asperities, barriers, characteristic earthquakes and strong motion prediction.

788   *Journal of Geophysical Research: Solid Earth*, 89(B7), 5867–5872.

789   Akyüz, S., Dogan, B., Aksoy, M. E., Tigli, O., & Zabci, C. (2014). *Preliminary*

790   *Palaeoseismological results of the Middle Strand of the North Anatolian Fault (NAF) in the*

791   *Marmara Region, NW Turkey.* Paper presented at European Geosciences Union General

792   Assembly, Vienna, Austria.

793   Akyüz, H. S., Hartleb, R., Barka, A., Altunel, E., Sunal, G., Meyer, B., & Armijo, R. (2002).

794   Surface rupture and slip distribution of the 12 November 1999 Düzce earthquake (M 7.1), North

795   Anatolian fault, Bolu, Turkey. *Bulletin of the Seismological Society of America*, 92(1), 61-66.

796   https://doi.org/10.1785/0120000840

797   Akyuz, H. S. & Zabci, C. (2012). *A review of paleoseismic investigations along the North*

798   *Anatolian Fault, Turkey.* Paper presented at PANAF: Paleoseismology Along the North

799   Anatolian Fault Meeting, Istanbul, Turkey.

800   Ambraseys, N. N. (1970). Some Characteristic Features of the Anatolian Fault Zone.

801   *Tectonophysics*, 9, 143-165. https://doi.org/10.1016/0040-1951(70)90014-4

802   Ambraseys, N. (2000). The Seismicity of the Marmara Sea Area 1800-1899. *Journal of*

803   *Earthquake Engineering,* 4(3), 377–401. https://doi.org/10.1080/13632460009350376

804   Ambraseys, N. N. (2001a). Reassessment of earthquakes, 1900–1999, in the eastern

805   Mediterranean and the Middle East. *Geophysical Journal International*, 145(2), 471–485.

806   https://doi.org/10.1046/j.0956-540x.2001.01396.x

807   Ambraseys, N. N. (2001b). The Earthquake of 1509 in the Sea of Marmara, Turkey, Revisited.

808   *Bulletin of the Seismological Society of America*, 91(6), 1397-1416.

809   https://doi.org/10.1785/0120000305

810   Ambraseys, N. (2002). The seismic activity of the Marmara Sea region over the last 2000 years.

811   *Bulletin of the Seismological Society of America*, 92(1), 1–18.

812   https://doi.org/10.1785/0120000843

813   Ambraseys, N. (2009). *Earthquakes in the Mediterranean and Middle East. A multidisciplinary*

814   *study of seismicity up to 1900.* Cambridge: Cambridge University Press.

815   https://doi.org/10.1017/CBO9781139195430

816   Ambraseys, N. & Finkel, C. (1991). Long-term seismicity of Istanbul and of the Marmara Sea

817   region. *Terra Nova*, 3(5), 527–539. https://doi.org/10.1111/j.1365-3121.1991.tb00188.x

818   Ambraseys, N. N., & Finkel, C. F. (1995). The Seismicity of Turkey and Adjacent Areas: A

819   Historical Review, 1500–1800. Istanbul: Muhittin Salih Eren.

820   Ambraseys, N. N., & Jackson, J. (1998). Faulting associated with historical and recent

821   earthquakes in the eastern Mediterranean region. *Geophysical Journal International*, 133(2),

822   390–406. https://doi.org/10.1046/j.1365-246X.1998.00508.x

823   Ambraseys, N.N., & Jackson, J.A. (2000). Seismicity of the Sea of Marmara (Turkey) since

824   1500. *Geophysical Journal International*, 141(3), F1-F6. https://doi.org/10.1046/j.1365-

825   246x.2000.00137.x

826   Ambraseys, N. N., Jackson, J. A., & Melville, C. P. (2002). Historical Seismicity and Tectonics:

827   The Case of the Eastern Mediterranean and the Middle East. In W. H. K. Lee, H. Kanamori, P.

828   C. Jennings, C. Kisslinger (Eds.). *International Handbook of Earthquake and Engineering*

829   *Seismology* (Part A, pp. 747-763). Cambridge, MA: Academic Press.

830   https://doi.org/10.1016/S0074-6142(02)80248-0

831   Ansberque, C., Bellier, O., Godard, V., Lasserre, C., Wang, M., Braucher, R., et al. (2016). The

832   Longriqu fault zone, eastern Tibetan Plateau: Segmentation and Holocene behavior. *Tectonics*,

833   35(3), 565–585.

834   Antoine, S. L., Klinger, Y., Delorme, A., Wang, K., Bürgmann, R., & Gold, R. (2021). Diffuse

835   Deformation and Surface Faulting Distribution from Submetric Image Correlation along the

836   2019 Ridgecrest, California, Ruptures. *Bulletin of the Seismological Society of America*,

837   https://doi.org/10.1785/0120210036

838   Armijo, R., Meyer, B., Hubert, A., & Barka, A. A. (1999). Westward propagation of the North

839   Anatolian fault into the northern Aegean: Timing and kinematics. *Geology*, 27, 267–270.

840   https://doi.org/10.1130/0091-7613(2000)28<188:WPONAF>2.0.CO;2

841   Armijo, R., Meyer, B., King, G. C. P., Rigo, A., & Papanastassiou, D. (1996). Quaternary

842   evolution of the Corinth Rift and its implications for the Late Cenozoic evolution of the Aegean.

843   *Geophysical Journal International*, 126(1), 11-53. https://doi.org/10.1111/j.1365-

844   246X.1996.tb05264.x

845   Armijo, R., Meyer, B., Navarro, S., King, G., & Barka, A. (2002). Asymmetric slip partitioning

846   in the Sea of Marmara pull-apart: a clue to propagation processes of the North Anatolian Fault?

847   *Terra Nova*, 14(2), 80–86. https://doi.org/10.1046/j.1365-3121.2002.00397.x

848   Arnold, M., Merchel, S., Bourlès, D. L., Braucher, R., Benedetti, L., Finkel, R. C., et al. (2010).

849   The French accelerator mass spectrometry facility ASTER: Improved performance and

850   developments. *Nuclear Instruments and Methods in Physics Research Section B: Beam*

851   *Interactions with Materials and Atoms*, 268, 1954-1959.

852   https://doi.org/10.1016/j.nimb.2010.02.107

853   Balco, G., Stone, J. O., Lifton, N. A., & Dunai, T. J. (2008). A complete and easily accessible

854   means of calculating surface exposure ages or erosion rates from ^{10}Be and ^{26}Al measurements.

855   *Quaternary Geochronology*, 3(3), 174 – 195. https://doi.org/10.1016/j.quageo.2007.12.001

856   Baris, S., Ito, A., Üçer, S. B., Honkura, Y., Kafadar, N., Pektas, R., et al. (2002).

857   Microearthquake Activity before the Izmit Earthquake in the Eastern Marmara region, Turkey (1

858   January 1993-17 August 1999). *Bulletin of the Seismological Society of America*, 92(1), 394–

859   405. https://doi.org/10.1785/0120000826

860   Barka, A. (1992). The North Anatolian fault zone. *Annales Tectonicae*, 6, 164–195.

861   Barka, A. (1993). *Kuzey Anadolu Fayı'nın Sapanca-Izmit ve Geyve-Iznik Kolları üzerinde*

862   *Palaeosismik Arastırmalar* (Technical Report YBAG-4/7551). Istanbul: TÜBITAK.

863   Barka, A. (1996). Slip distribution along the North Anatolian fault associated with the large

864   earthquakes of the period 1939 to 1967. *Bulletin of the Seismological Society of America*, 86(5),

865   1238–1254.

866   Barka, A., Akyüz, H. S., Altunel, E., Sunal, G., Cakir, Z., Dikbas, A., et al. (2002). The Surface

867   Rupture and Slip Distribution of the 17 August 1999 Izmit Earthquake (M 7.4), North Anatolian

868   Fault. *Bulletin of the Seismological Society of America*, 92(1), 43-60.

869   https://doi.org/10.1785/0120000841

870   Barka, A. & Kadinsky-Cade, K. (1988). Strike-slip fault geometry in Turkey and its influence on

871   earthquake activity. *Tectonics*, 7(3), 663–684.

872   Beauprêtre, S., Garambois, S., Manighetti, I., Malavieille, J., Sénéchal, G., Chatton, M., et al.

873   (2012). Finding the buried record of paste earthquakes with GPR-based palaeoseismology: a case

874   study on the Hope fault, New Zealand. *Geophysical Journal International*, 189(1), 73-100.

875   https://doi.org/10.1111/j.1365-246X.2012.05366.x

876   Beauprêtre, S., Manighetti, I., Garambois, S., Malavieille, J., & Dominguez, S. (2013).

877   Stratigraphic architecture and fault offsets of alluvial terraces at Te Marua, Wellington fault,

878   New Zealand, revealed by pseudo-3D GPR investigation. *Journal of Geophysical Research:*

879   *Solid Earth*, 118, 4564-4585.

880   Benjelloun, Y., de Sigoyer, Dessales, H., Baillet, L., Guéguen, P., & Sahin, M. (2020). Historical

881   Earthquake Scenarios for the Middle Strand of the North Anatolian Fault Deduced from Archeo-

882   Damage Inventory and Building Deformation Modeling. *Seismological Research Letters*, 92,

883   583-598. https://doi.org/10.1785/0220200278

884   Benjelloun, Y., de Sigoyer, J., Dessales, H., Garambois, S., & Sahin, M. (2018). Construction

885   history of the aqueduct of Nicaea (Iznik, NW Turkey) and its on-fault deformation viewed from

886   archaeological and geophysical investigations. *Journal of Archaeological Science: Reports*, 21,

887   389-400. https://doi.org/10.1016/j.jasrep.2018.08.010

888   Benjelloun, Y., de Sigoyer, J., Garambois, S., Carcaillet, J., & Klinger, Y. (2021). Data for:

889   Segmentation and Holocene Behavior of the Middle Strand of the North Anatolian Fault (NW

890   Turkey) (Version 1.2.0) [Data set]. Zenodo. http://doi.org/10.5281/zenodo.5566874

891   Broxton, M. J. & Edwards, L. J. (2008). *The Ames Stereo Pipeline: Automated 3D Surface

892   Reconstruction from Orbital Imagery*. Paper presented at the 39th Lunar and Planetary Science

893   Conference, League City, TX.

894   Brown, E. T., Edmond, J. M., Raisbeck, G. M., Yiou, F., Kurz, M. D., & Brook, E. J. (1991).

895   Examination of surface exposure ages of Antarctic moraines using in situ produced ^{10}Be and

896   ^{26}Al. *Geochimica et Cosmochimica Acta*, 55, 2269-2283. https://doi.org/10.1016/0016-

897   7037(91)90103-C

898   Chaput, E. (1936). *Voyages d'études géologique et géomorphogéniques en Turquie*. Paris : De

899   Boccard.

900   Chmeleff, J., von Blanckenburg, F., Kossert, K., & Jakob, D. (2010). Determination of the ^{10}Be

901   half-life by multicollector ICP-MS and liquid scintillation counting. *Nuclear Instruments and

902   Methods in Physics Research Section B: Beam Interactions with Materials and Atoms*, 268(2),

903   192–199. https://doi.org/10.1016/j.nimb.2009.09.012

904   Choi, J. H., Klinger, Y., Ferry, M., Ritz, J. F., Kurtz, R., Rizza, M. et al. (2018). Geologic

905   Inheritance and Earthquake Rupture Processes: The 1905 M ≥ 8 Tsetserleg-Bulnay Strike-Slip

906   Earthquake Sequence, Mongolia. *Journal of Geophysical Research: Solid Earth*, 123.

907   https://doi.org/10.1002/2017JB013962.

908   Civico, R., Smedile, A., Pantosti, D., Cinti, F. R., De Martini, P. M., Pucci, S., et al. (2021). New

909   trenching results along the Iznik segment of the central strand of the North Anatolian Fault

910   (Turkey): an integration with preexisting data. *Mediterranean Geoscience Reviews*, 3, 115-128.

911   https://doi.org/10.1007/s42990-021-00054-9

912   de Michele, M., Raucoules, D., de Sigoyer, J., Pubellier, M., & Chamot-Rooke, N. (2010).

913   Three-dimensional surface displacement of the 2008 May 12 Sichuan earthquake (China)

914   derived from Synthetic Aperture Radar: evidence for rupture on a blind thrust. *Geophysical*

915   *Journal International*, 183(3), 1097-1103. https://doi.org/10.1111/j.1365-246X.2010.04807.x

916   Dikbas, A., Akyüz, H. S., Meghraoui, M., Ferry, M., Altunel, E., Zabci, C., et al. (2018).

917   Paleoseismic history and slip rate along the Sapanca-Akyazi segment of the 1999 Izmit

918   earthquake rupture (MW=7.4) of the North Anatolian Fault (Turkey). *Tectonophysics*, 738-739,

919   92-111. https://doi.org/10.1016/j.tecto.2018.04.019

920   Dogan, B. (2010). *Kuzey Anadolu Fay Sistemi Güney Kolunun Geyve-Gemlik Arasindaki*

921   *Kesiminin Morfotektonik, Tektonostratigrafik ve Palaeosismolojik Evrimi*. (Doctoral

922   dissertation). Istanbul: Istanbul Teknik Üniversitesi.

923   Elliott, J. R., Walters, R. J., & Wright, T. J. (2016). The role of space-based observation in

924   understanding and responding to active tectonics and earthquakes. *Nature Communications*, 7,

925   13844. https://doi.org/10.1038/ncomms13844

926   Emre, Ö., Duman, T. Y., & Özalp, S. (2011*). 1:250.000 Ölçekli Türkiye Diri Fay Haritası Serisi*.

927   (Technical report). Ankara: Maden Tetkik ve Arama Genel Müdürlügü.

928   Erginal, A. E., Erenoglu, R. C., Yildirim, C., Selim, H., H., Kiyak, N. G, Erenoglu, O, et al.

929   (2021). Co-seismic beachrock deformation of 8th century CE Earthquake in Middle Strand of

930   North Anatolian Fault, Lake Iznik, NW Turkey. *Tectonophysics*, 799, 2286990.

931   https://doi.org/10.1016/j.tecto.2020.228690

932   Ergintav, S., Reilinger, R. E., Çakmak, R., Floyd, M., Cakir, Z., Dogan, U., et al. (2014).

933   Istanbul's earthquake hot spots: Geodetic constraints on strain accumulation along faults in the

934   Marmara seismic gap. *Geophysical Research Letters*, 41(16), 5783–5788.

935   https://doi.org/10.1002/2014GL060985

936   Flerit, F., Armijo, R., King, G. C. P., Meyer, B., & Barka, A. (2003). Slip partitioning in the Sea

937   of Marmara pull-apart determined from GPS velocity vectors. *Geophysical Journal*

938   *International*, 154(1), 1–7. https://doi.org/10.1046/j.1365-246X.2003.01899.x

939   Fletcher, J. M., Teran, O. J., Rockwell, T. K., Oskin, M. E., Hudnut, K., W., Mueller, K. J., et al.

940   (2014). Assembly of a large earthquake from a complex fault system: Surface rupture kinematics

941   of the 4 April 2010 El Mayor – Cucapah (Mexico) M$_w$ 7.2 earthquake. *Geosphere*, 10(4), 797-

942   827. https://doi.org/10.1130/GES00933.1

943   Fraser, J., Vanneste, K., & Hubert-Ferrari, A. (2010). Recent behavior of the North Anatolian

944   Fault: Insights from an integrated palaeoseismological data set. *Journal of Geophysical*

945   *Research: Solid Earth*, 115(B9): B09316.

946   Fu, B., Ninomiya, Y., Lei, X., Toda, S., & Awata, Y. (2004). Mapping active fault associated

947   with the 2003 Mw 6.6 Bam (SE Iran) earthquake with ASTER 3D images. *Remote Sensing of*

948   *Environment*, 92(2), 153–157. https://doi.org/10.1016/j.rse.2004.05.019

949   Gastineau, R., de Sigoyer, J., Sabatier, P., Fabbri, S. C., Anselmetti, F. S., Develle, A. L., et al.

950   (2021). Active subaquatic fault segments in Lake Iznik along the middle strand of the North

951   Anatolian Fault, NW Turkey. *Tectonics*, 40, e2020TC006404.

952   Gasperini, L., Polonia, A., Çagatay, M. N., Bortoluzzi, G., & Ferrante, V. (2011). Geological

953   slip rates along the North Anatolian Fault in the Marmara region. *Tectonics*, 30(6), TC6001.

954   Gold, P. O., Oskin, M. E., Elliott, A. J., Hinojosa-Corona, A., Taylor, M. H., Kreylos, O., &

955   Cowgill, E. (2013). Coseismic slip variation assessed from terrestrial lidar scans of the El

956   Mayor-Cucapah surface rupture. *Earth and Planetary Science Letters*, 366, 151-162.

957   https://doi.org/10.1016/j.epsl.2013.01.040

958   Grall, C., Henry, P., Thomas, Y., Westbrook, G.K., Çağatay, M.N., Marsset, B., et al. (2013).

959   Slip rate estimation along the western segment of the Main Marmara Fault over the last 405–490

960   ka by correlating mass transport deposits. *Tectonics*, 32, 2012TC003255.

961   doi:10.1002/2012TC003255.

962   Guidoboni, E., and Comastri, A. (Eds.) (2005). *Catalogue of Earthquakes and Tsunamis in the*

963   *Mediterranean Area From the 11th to the 15th Century*. Roma: Istituto Nazionale di Geofisica e

964   Vulcanologia.

965   Guidoboni, E., Comastri, A., & Traina, G. (1994). Catalogue of ancient earthquakes in the

966   Mediterranean area up to the 10th century. Roma: Istituto Nazionale di Geofisica.

967   Gürbüz, C., Aktar, M., Eyidogan, H., Cisternas, A., Haessler, H., Barka, A., et al. (2000). The

968   seismotectonics of the Marmara region (Turkey): results from a microseismic experiment.

969   *Tectonophysics*, 316(1), 1–17. https://doi.org/10.1016/S0040-1951(99)00253-X

970   Hamling, I. J., Hreinsdottir, S., Clark, K., Elliott, J., Liang, C., Fielding, E., et al. (2017).

971   Complex multifault rupture during the 2016 7.8 Kaikoura earthquake, New Zealand. *Science*,

972   356(6334), eaam7194. DOI: 10.1126/science.aam7194

973   Heisinger, B., Lal, D., Jull, A., Kubik, P., Ivy-Ochs, S., Knie, K., & Nolte, E. (2002a),

974   Production of selected cosmogenic radionuclides by muons: 2. capture of negative muons. *Earth*

975   *and Planetary Science Letters*, 200(3), 357 – 369. https://doi.org/10.1016/S0012-

976   821X(02)00641-6

977   Heisinger, B., Lal, D., Jull, A., Kubik, P., Ivy-Ochs, S., Neumaier, S., Knie, K., Lazarev, V., &

978   Nolte, E. (2002b). Production of selected cosmogenic radionuclides by muons: 1. fast muons.

979   *Earth and Planetary Science Letters*, 200(3), 345 – 355. https://doi.org/10.1016/S0012-

980   821X(02)00640-4

981   Hidy, A. J., Gosse, J. C., Pederson, J. L., Mattern, J. P., & Finkel, R. C. (2010). A geologically

982   constrained Monte Carlo approach to modeling exposure ages from profiles of cosmogenic

983   nuclides: An example from Lees Ferry, Arizona. *Geochemistry, Geophysics, Geosystems*, 11(9),

984   Q0AA10. https://doi.org/10.1029/2010GC003084

985   Honkura, Y. & Isikara, A. M. (1991). Multidisciplinary research on fault activity in the western

986   part of the North Anatolian Fault Zone. *Tectonophysics*, 193(4), 347–357.

987   https://doi.org/10.1016/0040-1951(91)90343-Q

988   Hubert-Ferrari, A., Barka, A., Jacques, E., Nalbant, S. S., Meyer, B., Armijo, R., et al. (2000).

989   Seismic hazard in the Marmara Sea region following the 17 August 1999 Izmit earthquake.

990   *Nature*, 404(6775), 269–273. https://doi.org/10.1038/35005054

991   Hubert-Ferrari, A., King., G., van der Woerd, J., Villa, I., Altunel, E., & Armijo, R. (2002).

992   Long-term evolution of the North Anatolian Fault: new constraints from its eastern termination.

993   In D. J. J. van Hinsbergen, M. A. Edwards, R. Govers (Eds.), *Collision and Collapse at the*

994   *Africa-Arabia-Eurasia Subduction Zone*, *Geological Society Special Publications* (Vol. 311, pp.

995 133-154). London: The Geological Society. doi: 10.1144/SP311.5

996 Hunter, J. D. (2007). Matplotlib: A 2D graphics environment. *Computing in Science &*

997 *Engineering*, 9, 90–95. https://doi.org/10.1109/MCSE.2007.55

998 Ikeda, Y. (1988). Recent activity of the Iznik-Mekece fault at Corak Stream, east of Iznik. In Y.

999 Honkura,A. M. Isikara (Eds.), *Multidisciplinary research on fault activity in the western part of*

1000 *the North Anatolian Fault Zone* (pp. 15–27). Tokyo: Institute of Technology.

1001 Ikeda, Y. (1988). Recent activity of the Iznik-Mekece fault at Corak Stream, east of Iznik. In Y.

1002 Honkura, A. M. Isikara (Eds.), *Multidisciplinary research on fault activity in the western part of*

1003 *the North Anatolian Fault Zone* (pp. 15–27). Tokyo: Institute of Technology.

1004 Ikeda, Y., Herece, E., Sugai, T., & Isikara, A. M. (1991). Postglacial crustal deformation

1005 associated with slip on the western part of the North Anatolian Fault Zone in the Iznik Lake

1006 Basin, Turkey. *Bulletin of the Department of Geography University of Tokyo*, 23, 13–23.

1007 Ikeda, Y., Suzuki, Y., & Herece, E. (1989). Late Holocene activity of the North Anatolian fault

1008 zone in the Orhangazi plain, northwestern Turkey. In Y. Honkura, A. M. Isikara (Eds.),

1009 *Multidisciplinary research on fault activity in the western part of the North Anatolian fault zone*

1010 (Vol. 2, pp. 16–30). Tokyo: Institute of Technology.

1011 Ikeda, Y., Suzuki, Y., Herece, E., Saroglu, F., Isikara, A. M., & Honkura, Y. (1991). Geological

1012 evidence for the last two faulting events on the north Anatolian Fault zone in the Mudurnu

1013 Valley, western Turkey. *Tectonophysics*, 193(4), 335-345. https://doi.org/10.1016/0040-

1014 1951(91)90342-P

1015 Ketin, I. (1969). Kuzey Anadolu Fayi Hakkinda. *Maden Tektik ve Arama Dergisi*, 72, 1-27.

1016 Ketin, I., & Rösli, F. (1953). Makroseismische Untersuchungen über das nordwest-anatolische

1017   Beben vom 18 März 1953. *Eclogae Geologicae Helvetiae*, 46, 187-208.

1018   Kim, S. J., Koh, K., Boyd, S., & Gorinevsky, D. (2009). l1 trend filtering. *SIAM Review*, 51(2),

1019   339-360. https://doi.org/10.1137/070690274

1020   King, G., & Nabelek, J. (1985). Role of Fault Bends in the Initiation and Termination of

1021   Earthquake Rupture. *Science,* 228(4702), 984-987. DOI: 10.1126/science.228.4702.984

1022   King., G., Klinger, Y., Bowman, D., & Tapponnier, P. (2005). Slip-Partitioned Surface Breaks

1023   for the M_w 7.8 2001 Kokoxili Earthquake, China. *Bulletin of the Seismological Society of*

1024   *America*, 95(2), 731-738. doi: 10.1785/0120040101

1025   Klinger, Y. (2010). Relation between continental strike-slip earthquake segmentation and

1026   thickness of the crust. *Journal of Geophysical Research: Solid Earth*, 115, B07306.

1027   Klinger, Y., Etchebes, M., Tapponnier, P., & Narteau, C. (2011). Characteristic slip for five great

1028   earthquakes along the Fuyun fault in China. *Nature Geoscience*, 4(6), 389–392.

1029   https://doi.org/10.1038/ngeo1158

1030   Klinger, Y., Sieh, K., Altunel, E., Akoglu, A., Barka, A., Dawson, T., et al. (2003).

1031   Palaeoseismic Evidence of Characteristic Slip on the Western Segment of the North Anatolian

1032   Fault, Turkey. *Bulletin of the Seismological Society of America*, 93(6), 2317-2332.

1033   https://doi.org/10.1785/0120010270

1034   Klinger, Y., Xu, X., Tapponnier, P., Van der Woerd, J., Lasserre, C., & King, G. (2005). High-

1035   Resolution Satellite Imagery Mapping of the Surface Rupture and Slip Distribution of the M_w

1036   ~7.8, 14 November 2001 Kokoxili Earthquake, Kunlun Fault, Northern Tibet, China. *Bulletin of*

1037   *the Seismological Society of America*, 95(5), 1970-1987. http://dx.doi.org/10.1785/0120040233

1038   Koçyigit, A. (1988). Tectonic setting of the Geyve Basin: age and total displacement of the

1039   Geyve Fault Zone. *Journal of Pure and Applied Sciences*, 21, 81–104.

1040   Koçyigit, A. & Özacar, A. A. (2003). Extensional neotectonic regime through the NE edge of the

1041   outer Isparta Angle, SW Turkey: new field and seismic data. *Turkish Journal of Earth Sciences*,

1042   12(1), 67–90.

1043   Kozaci, Ö., Dolan, J. F., & Finkel, R. C. (2009). A late Holocene slip rate for the central North

1044   Anatolian fault, at Tahtaköprü, Turkey, from cosmogenic [10]Be geochronology: Implications for

1045   fault loading and strain release rates. *Journal of Geophysical Research: Solid Earth*, 114(B1),

1046   B01405. https://doi.org/10.1029/2008JB005760

1047   Kozaci, Ö., Dolan, J. F., Finkel, R., & Hartleb, R. (2007). Late Holocene slip rate for the North

1048   Anatolian fault, Turkey, from cosmogenic 36Cl geochronology: Implications for the constancy

1049   of fault loading and strain release rates. *Geology*, 35(10), 867-870.

1050   https://doi.org/10.1130/G23187A.1

1051   Kürçer, A., Chatzipetros, A., Tutkun, S. Z., Pavlides, S., Özkan Ates, & Valkaniotis, S. (2008).

1052   The Yenice–Gönen active fault (NW Turkey): Active tectonics and palaeoseismology.

1053   *Tectonophysics*, 453(1), 263 – 275. https://doi.org/10.1016/j.tecto.2007.07.010

1054   Kürcer, A., Özalp, S., Özdemir, E., Uygun Güldogan, C., & Duman, T. Y. (2019). Active

1055   tectonics and paleoseismologic characteristics of the Yenice-Gönen fault, NW Turkey, in light of

1056   the 18 March 1953 Yenice-Gönen Earthquake (Ms=7.2). *Maden Tektik ve Arama Dergisi*, 159,

1057   29-62. https://doi.org/10.19111/bulletinofmre.500553

1058   Kurt, H., Sorlien, C.C., Seeber, L., Steckler, M.S., Shillington, D.J., Cifci, G., et al. (2013).

1059   Steady late quaternary slip rate on the Cinarcik section of the North Anatolian fault near Istanbul,

1060   Turkey. *Geophysical Research Letters*, 40, 4555-4559. doi:10.1002/grl.50882.

1061   Kurtz, R., Klinger, Y., Ferry, M., & Ritz, J. F. (2018). Horizontal surface-slip distribution

1062   through several seismic cycles: The Eastern Bogd fault, Gobi-Altai, Mongolia. *Tectonophysics*,

1063   734-735, 167-182. https://doi.org/10.1016/j.tecto.2018.03.011

1064   Lafarge, T., & Possolo, A. (2016). The NIST Uncertainty Machine. *NCSLI Measure*, 10(3), 20-

1065   27. DOI: 10.1080/19315775.2015.11721732

1066   Le Béon, M., Klinger, Y., Al-Qaryouti, M., Mériaux, A. S., Finkel, R., C., Elia, A., et al. (2010).

1067   Early Holocene and Late Pleistocene slip rates of the southern Dead Sea Fault determined from

1068   10Be cosmogenic dating of offset alluvial deposits. *Journal of Geophysical Research: Solid*

1069   *Earth*, 115, B11414, doi:10.1029/2009JB007198.

1070   Lefevre, M., Klinger, Y., Al-Qaryouti, M., Le Béon, M., & Moumani, K. (2018). Slip deficit and

1071   temporal clustering along the Dead Sea fault from palaeoseismological investigations. *Scientific*

1072   *Reports*, 8, doi:10.1038/s41598-018-22627-9.

1073   Le Pichon, X., Imren, C., Rangin, C., Sengör, A. M. C., & Siyako, M. (2014). The South

1074   Marmara Fault. *International Journal of Earth Sciences*, 103(1), 219–231.

1075   https://doi.org/10.1007/s00531-013-0950-0

1076   Lifton, N. (2016). Implications of two Holocene time dependent geomagnetic models for

1077   cosmogenic nuclide production rate scaling. *Earth and Planetary Science Letters*, 433, 257-268.

1078   https://doi.org/10.1016/j.epsl.2015.11.006

1079   Lifton, N. A., Sato, T., & Dunai, T. J. (2014). Scaling in situ cosmogenic nuclide production

1080   rates using analytical approximations to atmospheric cosmic-ray fluxes. *Earth and Planetary*

1081   *Science Letters*, 386, 149-160. https://doi.org/10.1016/j.epsl.2013.10.052

1082   Lin, Z., Liu-Zeng, J., Weldon II, R. J., Tian, J., Ding, C., & Du, Y. (2020). Modeling repeated

1083   coseismic slip to identify and characterize individual earthquakes from geomorphic offsets on

1084   strike-slip faults. *Earth and Planetary Science Letters*, 545, 116313.

1085   https://doi.org/10.1016/j.epsl.2020.116313

1086   Liu-Zeng, J., Klinger, Y., Sieh, K., Rubin, C., & Seitz, G. (2006). Serial ruptures of the San

1087   Andreas fault, Carrizo Plain, California, revealed by three-dimensional excavations. *Journal of*

1088   *Geophysical Research*, 111, B02306.

1089   Lozos, J. C. (2016). A case for historic joint rupture of the San Andreas and San Jacinto faults.

1090   *Science Advances*, 2(3), e1500621. https://doi.org/10.1126/sciadv.1500621

1091   Manighetti, I., Perrin, C., Dominguez, S., Garambois, S., Gaudemer, Y., Malavieille, J., et al.

1092   (2015). Recovering paleoearthquake slip record in a highly dynamic alluvial and tectonic region

1093   (Hope Fault, New Zealand) from airborne lidar. *Journal of Geophysical Research: Solid Earth*,

1094   120(6), 4484–4509. https://doi.org/10.1002/2014JB011787

1095   Manighetti, I., Perrin, C., Gaudemer, Y., Dominguez, S., Stewart, N., Malavieille, J., Garambois,

1096   S. (2020). Repeated giant earthquakes on the Wairarapa fault, New Zealand, revealed by Lidar-

1097   based paleoseismology. *Scientific Reports*, 10, 2124. https://doi.org/10.1038/s41598-020-59229-

1098   3

1099   Martin, L. C. P., Blard, P.-H., Balco, G., Lavé, J., Delunel, R., Lifton, N., Laurent, V. (2017).

1100   The CREp program and the ICE-D production rate calibration database: A fully parameterizable

1101   and updated online tool to compute cosmic-ray exposure ages. *Quaternary Geochronology*, 38,

1102   25-49. https://doi.org/10.1016/j.quageo.2016.11.006

1103   McClusky, S., Balassanian, S., Barka, A., Demir, C., Ergintav, S., Georgiev, I., et al. (2000).

1104   Global Positioning System constraints on plate kinematics and dynamics in the eastern

1105   Mediterranean and Caucasus. *Journal of Geophysical Research: Solid Earth*, 105(B3), 5695–

1106   5719.

1107   McGill, S. F., & Rubin, C. M. (1999). Surficial slip distribution on the central Emerson fault

1108   during the June 28, 1992, Landers earthquake, California. *Journal of Geophysical Research:*

1109   *Solid Earth*, 104(B3), 4811–4833.

1110   McGill, S. F., & Sieh, K. (1991). Surficial offsets on the Central and Eastern Garlock Fault

1111   associated with prehistoric earthquakes. *Journal of Geophysical Research*, 96(B13), 21597-

1112   21621.

1113   Meade, B. J., Hager, B. H., McClusky, S. C., Reilinger, R. E., Ergintav, S., Lenk, O., et al.

1114   (2002). Estimates of seismic potential in the Marmara Sea region from block models of secular

1115   deformation constrained by Global Positioning System measurements. *Bulletin of the*

1116   *Seismological Society of America*, 92(1), 208–215. http://dx.doi.org/10.1785/0120000837

1117   Merchel, S. & Herpers, U. (1999). An update on radiochemical separation techniques for the

1118   determination of long-lived radionuclides via accelerator mass spectrometry. *Radiochimica Acta*,

1119   84(4), 215-219. https://doi.org/10.1524/ract.1999.84.4.215

1120   Moratto, Z. M., Broxton, M. J., Beyer, R. A., Lundy, M., & Husmann, K. (2010). *Ames Stereo*

1121   *Pipeline, NASA's Open Source Automated Stereogrammetry Software*. Paper presented at the

1122   41th Lunar and Planetary Science Conference, Woodlands, TX.

1123   Motagh, M., Hoffmann, J., Kampes, B., Baes, M., & Zschau, J. (2007). Strain accumulation

1124   across the Gazikoy–Saros segment of the North Anatolian Fault inferred from Persistent

1125   Scatterer Interferometry and GPS measurements. *Earth and Planetary Science Letters*, 255, 432-

1126   444. http://dx.doi.org/10.1016/j.epsl.2007.01.003.

1127 Onderdonk, N., McGill, S., & Rockwell, T. (2018). A 3700 yr paleoseismic record from the

1128 northern San Jacinto fault and implications for joint rupture of the San Jancinto and San Andreas

1129 faults. *Geosphere*, 14(6), 2447-2468. https://doi.org/10.1130/GES01687.1

1130 Özalp, S., Emre, Ö., & Dogan, A. (2013). The segment structure of southern branch of the North

1131 Anatolian Fault and palaeoseismological behaviour of the Gemlik fault, NW Anatolia. *Bulletin of*

1132 *MTA*, 147, 1–17.

1133 Özbey, V., Özeren, M.S., Henry, P., Klein, E., Galgana, G., Karabulut, H., et al. (2021).

1134 Kinematics of the Marmara Region: a fusion of continuum and block models. *Mediterranean*

1135 *Geoscience Reviews*, 3, 57-78. https://doi.org/10.1007/s42990-021-00051-y

1136 Öztürk, K., Yaltirak, C., & Alpar, B. (2009). The relationship between the tectonic setting of the

1137 Lake Iznik Basin and the Middle Strand of the North Anatolian Fault. *Turkish Journal of Earth*

1138 *Sciences*, 18, 209–224.

1139 Palyvos, N., Pantosti, D., Zabci, C., & D'Addezio, G. (2007). Paleoseismological Evidence of

1140 Recent Earthquakes on the 1967 Mudurnu Valley Earthquake Segment of the North Anatolian

1141 Fault Zone. *Bulletin of the Seismological Society of America*, 97(5), 1646-1661.

1142 https://doi.org/10.1785/0120060049

1143 Parsons, T., Toda, S., Stein, R. S., Barka, A., & Dieterich, J. H. (2000). Heightened odds of large

1144 earthquakes near Istanbul: An interaction-based probability calculation. *Science*, 288(5466),

1145 661–665. https://doi.org/10.1126/science.288.5466.661

1146 Pondard, N., Armijo, R., King, G. C. P., Meyer, B., & Flérit, F. (2007). Fault interactions in the

1147 Sea of Marmara pull-apart (North Anatolian Fault): earthquake clustering and propagating

1148 earthquake sequences. *Geophysical Journal International*, 171, 1185-1197.

1149   https://doi.org/10.1111/j.1365-246X.2007.03580.x

1150   Reilinger, R., McClusky, S., Vernant, P., Lawrence, S., Ergintav, S., Cakmak, R., et al. (2006).

1151   GPS constraints on continental deformation in the Africa-Arabia-Eurasia continental collision

1152   zone and implications for the dynamics of plate interactions. *Journal of Geophysical Research:*

1153   *Solid Earth*, 111, B05411. doi:10.1029/2005JB004051.

1154   Reitman, N. G., Mueller, K. J., Tucker, G. E., Gold, R. D., Briggs, R. W., & Barnhart, K. R.

1155   (2019). Offset channels may not accurately record strike-slip fault displacements: Evidence from

1156   landscape evolution models. *Journal of Geophysical Research: Solid Earth*, 124, 13,427-13,451.

1157   Ren, Z., Zielke, O., & Yu, J. (2018). Active tectonics in 4D high-resolution. *Journal of*

1158   *Structural Geology*, 117, 264-271. https://doi.org/10.1016/j.jsg.2018.09.015

1159   Rizza, M., Ritz, J. F., Braucher, R., Vassallo, R., Prentice, C., Mahan, S., et al. (2011). Slip rate

1160   and slip magnitudes of past earthquakes along the Bogd left-lateral strike-slip fault (Mongolia).

1161   *Geophysical Journal International*, 186(3), 897-927. https://doi.org/10.1111/j.1365-

1162   246X.2011.05075.x

1163   Rockwell, T. K., Dawson, T. E., Young Ben-Horin, J., & Seitz, G. (2014). A 21-Event, 4,000

1164   Year History of Surface Ruptures in the Anza Seismic Gap, San Jacinto Fault, and Implications

1165   for Long-term Earthquake Production on a Major Plate Boundary Fault. *Pure and Applied*

1166   *Geophysics*, 172, 1143-1165. https://doi.org/10.1007/s00024-014-0955-z

1167   Rockwell, T. K., Lindvall, S., Dawson, T., Langridge, R., Lettis, W., & Klinger, Y. (2002).

1168   Lateral Offsets on Surveyed Cultural Features Resulting from the 1999 Izmit and Düzce

1169   Earthquakes, Turkey. *Bulletin of the Seismological Society of America*, 92(1), 79-94.

1170   https://doi.org/10.1785/0120000809

1171 Rockwell, T., Ragona, D., Seitz, G., Langridge, R., Ersen Aksoy, M., Ucarkus, G., et al. (2009).

1172 Palaeoseismology of the North Anatolian Fault near the Marmara Sea: Implications for fault

1173 segmentation and seismic hazard. In K. Reicherter, A. M. Michetti, P. G. Silva (Eds.),

1174 *Palaeoseismology: Historical and Prehistorical Records of Earthquake Ground Effects for*

1175 *Seismic Hazard Assessment*, *Geological Society Special Publications* (Vol. 316(1), pp. 31-54).

1176 London: The Geological Society. https://doi.org/10.1144/SP316.3

1177 Scharer, K. M., Salisbury, J. B., Arrowsmith, J. R., & Rockwell, T. K. (2014). Southern San

1178 Andreas Fault Evaluation Field Activity: Approaches to Measuring Small Geomorphic Offsets –

1179 Challenges and Recommendations for Active Fault Studies. *Seismological Research Letters*, 85,

1180 68-76. https://doi.org/10.1785/0220130108

1181 Schwartz, D. P., & Coppersmith, K. J. (1984). Fault Behavior and Characteristic Earthquakes:

1182 Examples From the Wasatch and San Andreas Fault Zones. *Journal of Geophysical Research*,

1183 89(B7), 5681-5698.

1184 Sengör, A. M. C., Grall, C., Imren, C., Le Pichon, X., Görür, N., Henry, P., et al. (2014). The

1185 geometry of the North Anatolian transform fault in the Sea of Marmara and its temporal

1186 evolution: implications for the development of intracontinental transform faults. *Canadian*

1187 *Journal of Earth Sciences*, 51(3), 222–242. https://doi.org/10.1139/cjes-2013-0160

1188 Sengör, A. M. C., Tüysüz, O., Imren, C., Sakinç, M., Eyidogan, H., Görür, N., et al. (2005). The

1189 North Anatolian Fault: A New Look. *Annual Review of Earth and Planetary Sciences*, 33, 37-

1190 112. https://doi.org/10.1146/annurev.earth.32.101802.120415

1191 Sengör, A. M. C., & Zabci, C. (2019). The North Anatolian Fault and the North Anatolian Shear

1192 Zone. In C. Kuzucuoglu, A. Ciner, N. Kazanci (Eds.), *Landscape and Landforms of Turkey* (pp.

1193   481-494). Cham: Springer International Publishing. https://doi.org/10.1007/978-3-030-03515-

1194   0_27

1195   Shean, D. E., Alexandrov, O., Moratto, Z., Smith, B. E., Joughin, I. R., Porter, C. C., & Morin, P.

1196   J. (2016). An automated, open-source pipeline for mass production of digital elevation models

1197   (DEMs) from very high-resolution commercial stereo satellite imagery. *ISPRS Journal of*

1198   *Photogrammetry and Remote Sensing*, 116, 101–117.

1199   https://doi.org/10.1016/j.isprsjprs.2016.03.012

1200   Sieh, K. E. & Jahns, R. H. (1984). Holocene activity of the San Andreas fault at Wallace Creek,

1201   California. *Geological Society of America Bulletin*, 95(8), 883–896.

1202   https://doi.org/10.1130/0016-7606(1984)95<883:HAOTSA>2.0.CO;2

1203   Sipahioglu, S. & Matsuda, T. (1986). Geology and Quaternary fault in the Iznik-Mekece area. In

1204   A. M. Isikara, Y. Honkura (Eds.), *Electric and Magnetic Research on Active Faults in the North*

1205   *Anatolian Fault Zone*. (pp. 25-41). Tokyo: Tokyo Inst. Technology.

1206   Stein, R. S., Barka, A. A., & Dieterich, J. H. (1997). Progressive failure on the North Anatolian

1207   fault since 1939 by earthquake stress triggering. *Geophysical Journal International*, 128(3), 594–

1208   604. https://doi.org/10.1111/j.1365-246X.1997.tb05321.x

1209   Straub, C., Kahle, H.-G., & Schindler, C. (1997). GPS and geologic estimates of the tectonic

1210   activity in the Marmara Sea region, NW Anatolia. *Journal of Geophysical Research: Solid*

1211   *Earth*, 102(B12), 27587–27601.

1212   Stroeven, A. P., Heyman, J., Fabel, D., Björck, S., Caffee, M. W., Fredin, O., & Harbor, J. M.

1213   (2015). A new Scandinavian reference ^{10}Be production rate. *Quaternary Geochronology*, 29,

1214   104–115. https://doi.org/10.1016/j.quageo.2015.06.011

1215 Tanoglu, A., & Erinc, S. (1956). Garsak bogazı ve Eski Sakarya (The Garsak gorge and the

1216 Sakarya River diversion). *Istanbul Universitesi Cografya Enstitusu Dergisi*, 4, 17–31.

1217 Tsukuda, T., Satake, K., Honkura, Y., Üçer, S. B., & Isikara, A. M. (1988). Low seismicity, low

1218 coda-Q and discontinuities of the upper crust in the vicinity of the Iznik-Mekece fault, the North

1219 Anatolian Fault Zone, Turkey. *Bulletin of Earthquake Research of the Institute University of*

1220 *Tokyo*, 63, 327–348.

1221 Uppala, S. M., KÅllberg, P. W., Simmons, A. J., Andrae, U., Bechtold, V. D. C., Fiorino, M., et

1222 al. (2005). The ERA-40 re-analysis. *Quarterly Journal of the Royal Meteorological Society*, 131,

1223 2961-3012. https://doi.org/10.1256/qj.04.176

1224 van der Woerd, J., Klinger, Y., Sieh, K., Tapponnier, P., Ryerson, F. J., & Mériaux, A. S. (2006).

1225 Long-term slip rate of the southern San Andreas Fault from ^{10}Be-^{26}Al surface exposure dating of

1226 an offset alluvial fan. *Journal of Geophysical Research*, 111, B04407.

1227 Vardar, D., Öztürk, K., Yaltırak, C., Alpar, B., & Tur, H. (2014). Late Pleistocene-Holocene

1228 evolution of the southern Marmara shelf and sub-basins: middle strand of the North Anatolian

1229 fault, southern Marmara Sea, Turkey. *Marine Geophysical Research*, 35(1), 69-85.

1230 https://doi.org/10.1007/s11001-013-9210-8

1231 Ward, S. N. (1997). Dogtails versus rainbows: synthetic earthquake rupture models as an aid in

1232 interpreting geological data. *Bulletin of the Seismological Society of America*, 87(1), 1422-1441.

1233 Wechsler, N., Rockwell, T. K., & Klinger, Y. (2018). Variable slip-rate and slip-per-event on a

1234 plate boundary fault: The Dead Sea fault in northern Israel. *Tectonophysics*, 722, 210-226.

1235 https://doi.org/10.1016/j.tecto.2017.10.017

1236 Wells, D. L., & Coppersmith, K. J. (1994). New Empirical Relationships among Magnitude,

1237   Rupture Length, Rupture Width, Rupture Area, and Surface Displacement. *Bulletin of the*

1238   *Seismological Society of America*, 84(4), 974-1002.

1239   Wesnousky, S. G. (2006). Predicting the endpoints of earthquake ruptures. *Nature*, 444, 358-360.

1240   https://doi.org/10.1038/nature05275

1241   Yılmaz, Y., Genç, C., Yigitbas, E., Bozcu, M., & Yılmaz, K. (1995). Geological evolution of the

1242   late Mesozoic continental margin of Northwestern Anatolia. *Tectonophysics*, 243(1), 155–171.

1243   https://doi.org/10.1016/0040-1951(94)00196-G

1244   Yoshioka, T. & Kusçu, I. (1994). Late Holocene faulting events on the Iznik-Mekece fault in the

1245   western part of the North Anatolian fault zone, Turkey. *Bulletin of the Geological Survey of*

1246   *Japan*, 45(11), 677–685.

1247   Zabcı, C. (2019). Spatio-temporal behaviour of continental transform faults: Implications from

1248   the late Quaternary slip history of the North Anatolian Fault, Turkey. *Canadian Journal of Earth*

1249   *Sciences*, 56(11), 1218-1238. https://doi.org/10.1139/cjes-2018-0308

1250   Zabci, C., Sançar, T., Akyüz, H. S., & Kiyak, N. G. (2015). Spatial slip behavior of large strike-

1251   slip fault belts: Implications for the Holocene slip rates of the eastern termination of the North

1252   Anatolian Fault, Turkey. *Journal of Geophysical Research: Solid Earth*, 120(12), 8591-8609.

1253   Zielke, O. (2018). Earthquake Recurrence and the Resolution Potential of Tectono-Geomorphic

1254   Records. *Bulletin of the Seismological Society of America*, 108(3A), 1399-1413.

1255   https://doi.org/10.1785/0120170241

1256   Zielke, O., Arrowsmith, J. R., Grant Ludwig, L., & Akçiz, S. O. (2010). Slip in the 1857 and

1257   earlier large earthquakes along the Carrizo Plain, San Andreas Fault. *Science*, 327, 1119-1122.

1258   https://doi.org/10.1126/science.1182781

1259   Zielke, O., Arrowsmith, J. R., Grant Ludwig, L., & Akciz, S. O. (2012). High-Resolution

1260   Topography-Derived Offsets along the 1857 Fort Tejon Earthquake Rupture Trace, San Andreas

1261   Fault. *Bulletin of the Seismological Society of America*, 102(3), 1135-1154.

1262   https://doi.org/10.1785/0120110230

1263   Zielke, O., Klinger, Y., & Arrowsmith, J. R. (2015). Fault slip and earthquake recurrence along

1264   strike-slip faults - Contributions of high-resolution geomorphic data. *Tectonophysics*, 638, 43–

1265   62. https://doi.org/10.1016/j.tecto.2014.11.004

1266